Extension of a Local Correlation-Based Transition Model in OpenFOAM

Boris Kruljevic

School of Engineering

Thesis submitted for examination for the degree of Master of Science in Technology.

Espoo 22.4.2016

Thesis supervisor:

Prof. Jukka Tuhkuri

Thesis advisors:

Prof. Timo Siikonen

Dr. Mizanur Rahman

Aalto University
School of Engineering

AALTO UNIVERSITY
SCHOOL OF ENGINEERING

ABSTRACT OF THE
MASTER'S THESIS

Author: Boris Kruljevic

Title: Extension of a Local Correlation-Based Transition Model in OpenFOAM

Date: 22.4.2016 Language: English Number of pages: 8+56

Department of Applied Mechanics

Professorship: Fluid Mechanics

Supervisor: Prof. Jukka Tuhkuri

Advisors: Prof. Timo Siikonen, Dr. Mizanur Rahman

Depending on the flow regimes, which can be laminar or turbulent, important characteristics of the flow can differ quite significantly. The ability to predict which regime will take place is important in many engineering applications of fluid mechanics. In order to predict transition, most often numerical methods have to be used or a branch of fluid mechanics, known as computational fluid dynamics (CFD). The problem with many transition models, is that the use of non-local variables is needed, such as following certain quantities along streamlines, which makes it difficult to use such models for general CFD codes, where the computation of non-local variables is problematic. In this work, a local correlation-based model is employed, which avoids the deficiencies of these previous transition models. The model is not based on physics, but empirical correlations. Since many factors affect transition, the original model did not include all of them. It is the aim of this thesis to extend the transition model, already implemented in the software OpenFOAM, to include crossflow- and roughness-induced transition prediction capabilities, which were found in different publications. The model which included the roughness extension was tested on flat plate cases, with zero-, favorable- and adverse-pressure gradients. The crossflow-extended model, was tested on the Onera M6 wing, at different angles of attack. Although the results are promising and the models show a correct behaviour, there was no very close agreement in different cases for both roughness- and crossflow-extended models. The reason could be the manner in which the transition model was implemented in OpenFOAM.

Keywords: Transition, Turbulence, OpenFOAM, CFD, RANS

Preface

The topic of a turbulent flow is something I became very interested in, and wanted to gain a deeper understanding. Through the making of this thesis, I have learned a great deal about turbulence and turbulence modelling, physics of transition and many other topics concerning the physical and numerical aspects of fluid mechanics.

I would like to thank Professor Jukka Tuhkuri, Professor Timo Siikonen and Dr. Mizanur Rahman, who were my supervisors and advisors, in this work. Furthermore, I would like to express my gratitude to Professor Siikonen for guiding me through my studies, always ready to give his time, and clear up any misunderstandings I had with different topics of fluid mechanics. Also, for appointing my as a course assistant for two computational fluid dynamics course, which greatly contributed in my development and understanding of the field. I would also like to express my gratitude to all my friends who supported me in this project, as well as to my family for their contribution. Finally, I would like to thank the Aalto University for accepting me as guest student in the spring semester of 2013, and later on as a full time student. I had a very pleasant experience at this university and Finland as a whole.

Otaniemi, 22.4.2016

Boris Kruljevic

Contents

Symbols and abbreviations

Roman Symbols

A_r	roughness amplification factor
C_f	skin friction coefficient
C_μ	turbulence model coefficient
E	coefficient in the log-law, total energy per mass unit
F_{length}	length of the transition zone
H	helicity
Kn	Knudsen number
k	turbulence kinetic energy
k_s	equivalent sand grain roughness height
k^+	equivalent sand grain roughness
L	characteristic length scale
$\mathbf{r}$	distance vector
Re_{ks}	equivalent sand grain roughness height Reynolds number
Re	Reynolds number
Re_H	Reynolds number based on a local helicity
Re_v	strain rate / vorticity Reynolds number
Re_θ	momentum thickness Reynolds number
$Re_{\theta c}$	critical momentum thickness Reynolds number
$Re_{\theta t}$	transition onset momentum thickness Reynolds number
$\tilde{Re}_{\theta t}$	local transition onset momentum thickness Reynolds number
R_T	viscosity ratio
R_y	wall distance based turbulence Reynolds number
s	streamwise direction
S	absolute value of the strain rate
$\mathbf{S}$	face-area vector
Tu	turbulence instensity
Tu_{ff}	freestream turbulence intensity
p	pressure
q	source term
$\mathbf{U}$	velocity vector
u_∞	freestream velocity
u^+	dimensionless velocity
u_τ	friction velocity
$\overline{u}$	RANS averaged velocity
u'	fluctuating velocity component
y	distance from the wall
y^+	dimensionless wall distance

Greek Symbols

α	diffusion coefficient
γ	intermittency
γ_{eff}	effective intermittency
Δ	change
δ^*	displacement thickness
δ_{ij}	Kronecker delta
ϵ	dissipation of turbulent kinetic energy
θ	momentum thickness
λ_θ	Thwaites parameter, pressure gradient parameter
μ	dynamic viscosity
μ_τ	turbulent dynamic viscosity
ν	kinematic viscosity
ν_τ	kinematic eddy viscosity
ϕ	scalar
σ_{ij}	stress tensor
σ_k	Schmidt number for k
σ_ϵ	Schmidt number for ϵ
σ_ω	Schmidt number for ω
ρ	density
τ_w	wall shear stress
ω	specific Dissipation Rate
ω_{rough}	ω boundary condition for rough surfaces
ω_{smooth}	ω boundary condition without roughness
$\boldsymbol{\omega}$	vorticity vector

Operators

$\nabla \cdot \mathbf{A}$	divergence
$\frac{\partial}{\partial t}$	partial derivative with respect to variable t
$\sum_i$	sum over index i
$\mathbf{A} \cdot \mathbf{B}$	dot product of vectors $\mathbf{A}$ and $\mathbf{B}$

Abbreviations

CFD	Computational fluid dynamics
DNS	Direct numerical simulations
FSTI	Freestream turbulence intensity
FVM	Finite-volume method
GAMG	Geometrics Algebraic Multigrid Method
LES	Large eddy simulations
PBiCG	Preconditioned Biconjugate Gradient
PISO	Pressure-Implicit with Splitting of Operator
RANS	Reynolds-averaged Navier-Stokes
SIMPLE	Semi-Implicit Method for Pressure-Linked Equations

1 Introduction

The ability to predict laminar to turbulent transition is important in many engineering applications of fluid mechanics. Depending on the flow regimes, whether laminar or turbulent, important characteristics, such as wall shear stress, heat transfer and flow separation behaviour could differ quite significantly. In gas turbines, for example, the blades are cooled to prevent failure. If the transition is predicted incorrectly, overheating or overcooling could then occur. Similarly, extensive regions of laminar and turbulent flow exist on an aircraft. In aircraft design, the reduction of drag is a top priority, which could be achieved by delaying laminar to turbulent transition. Sometimes, however, turbulent flow is desired, as flow separation is then delayed for higher angles of attack, and the aircraft is able to land at a lower, safer speed.

In order to predict transition, most often, numerical methods have to be used, or the branch of fluid mechanics known as Computational Fluid Dynamics (CFD). CFD emerged in the 1960's as a result of a combination of advances in computer power and algorithms. Before, experimental and theoretical methods have been used in the design of equipment and vehicles involving fluid flow and heat transfer. Among the most popular methods in CFD is the finite-volume method, employed also in this work. Using this method, the domain of interest is decomposed into a number of elements, called control volumes, thus creating a grid or mesh, and the partial differential equations are turned into algebraic expressions by integration over the control volumes. Although CFD is a very powerful tool, simulations of complicated physical process can be quite expensive, depending on the mesh size, and different characteristics of the problems (unsteady flow, chemical reactions, turbulence...), resulting in simulations that can take a very long time. The trend is, however, toward greater reliance on computer-based prediction in design. Economics plays the main role, as computer speed increases continuously, and the cost of performing a given calculation decreases. In order to decrease the cost of computation, there are various simplifications that are made by the user. The physically correct and general mathematical model for almost all engineering purposes is a highly nonlinear system of partial differential equations known as the Navier-Stokes equations. The influence of such nonlinearities is most often seen in turbulent flows, which is the most common flow regime found in nature. They are highly vortical, and fluctuating down to very small scales in space and time [1].

As turbulent flow consists of a wide range of different scales, the computational demand to simulate all these scales is extremely high. For this reason, turbulence has to be filtered, to different degrees, in almost all engineering flow problems. Depending on the level of approximation, turbulence computation can be roughly classified into Direct Numerical Simulation (DNS), Large Eddy Simulation (LES) and Reynolds-averaged Navier-Stokes (RANS) methods. The DNS methods are the most accurate, but also the most computationally expensive since no filtering is applied. In the LES, some spatial filtering is applied, and those scales, which are not computed directly, are then modelled. The Reynolds-averaged Navier-Stokes approach is the

most commonly used in the industry, since it is the least computationally demanding. The Navier-Stokes equations are averaged in time, and all turbulent scales are modelled.

At present, there are many different methods to simulate transition. DNS and LES can be used to predict transition quite accurately, at least in principle [2]. These methods are, as mentioned, the most computationally expensive and at the moment, their application for practical engineering use for transition prediction is out of reach. Using the RANS approach, the simplest models are the so called *low-Re* models. which have been used with some degree of success. However, their performance was found to be unsatisfactory, and their success was argued to be accidental [3]. An alternative is to use methods based on the linear stability theory, of which the most widely used it the e^n method, and coupling it with a RANS solver. There are issues, however, in using this method with unstructured grids, which are used the most often for complex problems, where building of a structured grid would take a very long time. In a structured grid, the neighbourhood relationships are defined by storage arrangement, which makes it possible to track certain quantities along streamlines, which is done in the e^n method. The use of empirical relations has the same issue, since certain quantities, which are non-local in the flow are needed, and therefore, again the use of these methods for unstructured grids is problematic.

A fully CFD-compatibly transition model should posses the following features [2]:

1. Allow the *calibrated* prediction of onset and the length of transition
2. Allow the inclusion of different transition mechanisms
3. Be formulated locally (no search or line-integration operations)
4. Avoid multiple solutions (same solution for initially laminar or turbulent boundary layer)
5. Do not affect the underlying turbulence model in fully turbulent regimes
6. Allow a robust integration down to the wall with similar convergence as the underlying turbulence model
7. Be formulated independent of the coordinate system
8. Applicable to three-dimensional boundary layers

In 2002, a new transition model, based on the RANS method, was developed by Menter et al. [4], that only required the use of local variables, avoiding the deficiencies of the previous models. Then in 2006, a model was published by Langtry [2], using some ideas from Menter's paper. The physics is captured by the empirical correlations, and the use of non-local operations is avoided. There are also models for transition being developed that are phenomenological, and based on local variables, however, these models are used less, since the physics of transition is still not entirely understood,

and is an active area of research. For this reason, some authors have argued that correlation-based models are more appropriate candidates for consistent RANS-based transition prediction than their physics-based counterparts [3]. Langtry's model has a number of deficiencies, such as the lack of Galilean invariance. A new version was published in 2015 by Menter et al. [5], where the Galilean invariance deficiency was removed, and in the future, the focus is likely going to be on this model.

As transition depends on many factors, not all are present in the original model by Langtry. It has been extended for different correlations by a number of authors since the publication, and in this work, the effects of roughness and crossflow-induced transition, based on the works by authors Langel and Chow for roughness [6] and authors Müller and Herbst, for crossflow-induced transition [7], are introduced in the original model, which has already been implemented in OpenFOAM.

In this thesis, the background of the boundary layer theory and transition is given in Chapter 2. The different factors affecting transition are discussed in the next chapter. Chapter 4 deals with the governing equations in this work, including turbulence modelling. The numerical methods, such as discretization and solution methodology are also covered. The transition model is described in detail in Chapter 5, along with the extensions. This is followed by the test cases, beginning with the roughness model, which is tested on some flat plate cases, with and without the pressure gradient. After that, the Onera M6 case is covered, for the crossflow effects in Chapters 6 and 7, respectively. Finally, conclusions are drawn.

2 Boundary Layer Principles and Transition

In fluid mechanics we can distinguish between viscous and inviscid flows. The classification is based on the effects of viscosity, which is a quantity that describes a fluid's resistance to flow. Fluids have the property to resist the relative motion of immersed objects through them as well as the motion of layers with differing velocities within them. The difference between inviscid and viscous flow is simply that the latter takes viscosity into consideration, while the former does not. The inviscid flow is just an assumption to simplify calculations, and it is important to be aware when it can be applied in the analysis.

For a long time, the importance of viscosity in solving fluid mechanics problems was underestimated. The value of viscosity for the two most significant fluids, air and water, is very low, and so it was believed that its effect and the forces of viscous friction are small. This assumption was wrong and the theoretical results of the Euler's inviscid equations were quite different than what was observed in the experiments. A major problem at the time, was that the equations involving viscosity, the Navier-Stokes equations, were very complicated to solve. At the beginning of the 20th century, L. Prandtl proved that the flow about a solid can be divided into two regions, a very thin layer in the vicinity of the body, called a *boundary layer* and the outside region, where friction can be neglected. He was able to simplify the mathematics and took the first step toward the reunification of theory and practice. The boundary-layer theory provided the tools for the development of fluid dynamics [8].

A important application of the boundary-layer theory is that it is used in the calculations of skin-friction drag, which cannot be done using the inviscid assumption, such as in the case of the Euler equations. The boundary layer principles are also used in determining flow separation which greatly affects the pressure distribution. While the potential theory, which assumes an inviscid flow, is used in determining the pressure distribution over airfoils or wings, once separation occurs, the potential theory can no longer be applied by itself.

2.1 Flow Regimes and Boundary Layer

A boundary layer on a flat plate is shown on Figure 1. The fluid, due to viscosity, sticks to the wall, and the velocity relative to the wall is zero. An increase in the streamwise flow velocity can be observed away from the wall, until it is equal to the freestream velocity u_∞. Considering viscous flow, we can distinguish two regimes, the laminar and turbulent. At a high enough Reynolds number, a laminar flow will turn into a turbulent one. The Reynolds number relates the viscous and inertial forces, and if small perturbation are damped out by the viscosity, the flow will remain laminar. The Reynolds number is given by:

$$Re = \frac{\rho u_\infty L}{\mu} \tag{1}$$

where ρ is the density, u_∞ the freestream velocity, L is a characteristic length of the object and μ the dynamic viscosity of the fluid.

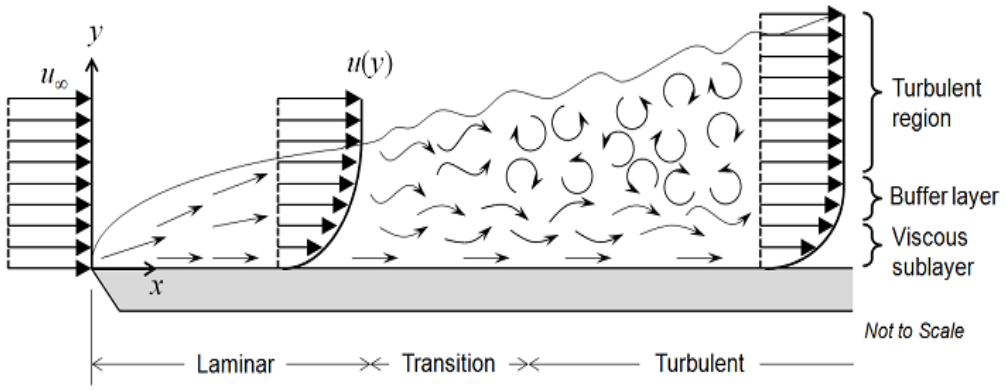

Figure 1: Flat plate boundary layer [9].

Laminar and turbulent regimes have an important distinction. When fluids are slow and have a high viscosity, the flow tends to be laminar at the resulting low Reynolds number. It is characterized by layers, or laminas, of air moving at the same velocity. The lines are parallel, smooth and the laminas are not interacting. Observing turbulent flow, chaotic movement can be seen. The flow lines are disorganized, and the flow structure compromised of eddies varying in a wide range of scale. This enhances mixing, increases the heat transfer and makes the turbulent flow very useful in various applications. The turbulent flow will, however, result in higher drag, which in most applications is unwanted. This can be explained with Figure 2, where the difference between the laminar and turbulent boundary layer streamwise velocity profile is shown.

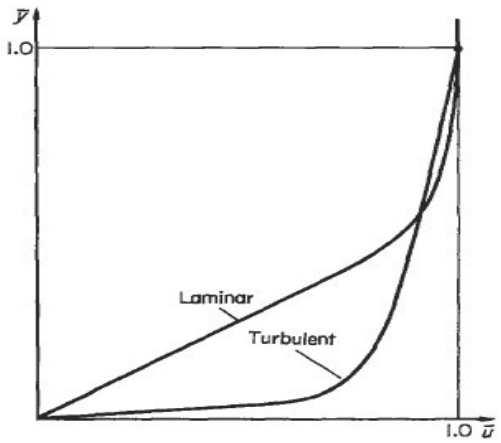

Figure 2: Laminar and turbulent velocity profiles [10].

Compared to laminar flow, the boundary layer tends to be bigger in turbulent flows and the friction higher, due to a higher gradient at the wall.

The turbulent boundary layer can be divided into different regions, with different characteristics. Understanding these regions is important in turbulent flow computation. The turbulent boundary layer is shown in Figure 3.

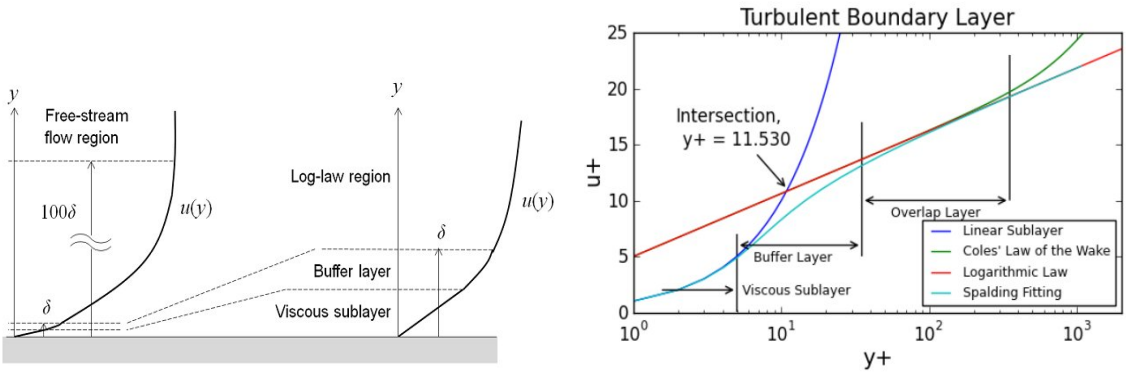

Figure 3: Turbulent boundary layer [9, 11].

The boundary layer can be divided in three parts. The division is based on the following non-dimensional quantities: a dimensionless velocity (u^+) and a dimensionless distance from the wall (y^+). These quantities are defined as:

$$u^+ = \frac{U}{u_\tau}, \qquad y^+ = \frac{y u_\tau}{\nu} \tag{2}$$

where U is the velocity parallel to the wall as a function of y, which is the distance from the wall and ν is the kinematic viscosity. The friction velocity, u_τ, is given by:

$$u_\tau = \sqrt{\frac{\tau_w}{\rho}} \tag{3}$$

where τ_w is the shear stress at the wall. The friction velocity is defined as a velocity scale which is based on the friction force at the wall. The overlap layer or log-layer obeys a logarithmic relationship with the distance from the wall. The zone is approximately from $y^+ = 35$ to $y^+ = 350$. In the log-layer, the velocity profile is:

$$u^+ = \frac{1}{\kappa} \ln (E y^+) \tag{4}$$

where $\kappa = 0.4$ is the Von Kármán constant and $E = 9.8$. The viscous sublayer, which is closest to the surface, and takes the zone from the wall to about $y^+ \leq 5$ is dominated by viscous effects resulting in a velocity profile $u^+ = y^+$. In the buffer layer, the velocity does not obey either of these laws. A fitting that matches data in all of the three regions, and well up to the outermost part of the boundary layer, has been proposed by Spalding [12].

Two important quantities of the boundary layer are the displacement thickness δ^* and momentum thickness θ. For a compressible boundary layer, they are defined as [12]:

$$\delta^* = \int_0^\infty \left(1 - \frac{\rho}{\rho_e}\frac{u}{u_e}\right) dy \tag{5}$$

$$\theta = \int_0^\infty \frac{\rho}{\rho_e}\frac{u}{u_e}\left(1 - \frac{u}{u_e}\right) dy \tag{6}$$

Physically, the momentum thickness represents the loss of momentum compared to a potential (inviscid) flow, inside the boundary layer. The displacement thickness is the disturbance over which the streamlines outside the boundary layer are shifted due to presence of the boundary layer. The momentum thickness Reynolds number can be formulated as:

$$Re_\theta = \frac{u_e \theta}{\nu} \tag{7}$$

where u_e is the velocity at the edge of the boundary layer. This quantity is important in transition modelling, and will be used in the local correlation-based transition model applied in this work. The shape factor H is defined as the ratio of the displacement thickness and momentum thickness:

$$H = \frac{\delta^*}{\theta} \tag{8}$$

The shape factor can be used a criterion for separation [12].

2.2 Transition to Turbulence

The flow does not become turbulent instantly, but undergoes a transition process. Due to external factors, such as a pressure gradient, a surface curvature, roughness, instabilities can develop in a laminar boundary layer causing the transition. The process is called laminar-to-turbulent transition. Typically, the point of minimum friction is the start of transition. The process is considered completed, once the skin friction reaches its fully turbulent value. Transition extend is the region between the start and end of the process. [13]

Morkovin [14] introduced the concept of receptivity, to describe the way in which a certain external disturbance enters the boundary layer and the nature of its signature in the perturbed flow. Depending on a number of factors, different instabilities can develop, together or independently. As the response amplitude grows, nonlinear interactions can occur in the form of secondary instabilities before reaching breakdown phase. In an otherwise 2D flow, the breakdown phase is a 3D phenomenon. It is characterized by a formation of intermittent turbulent spots that grow at a constant rate and independent of each other. The intermittency factor was introduced to quantify the rate of turbulent spot production. Once they are formed, these spots grow in size as they travel downstream. Eventually they merge into a fully turbulent boundary layer, and the transition process is complete. [13]

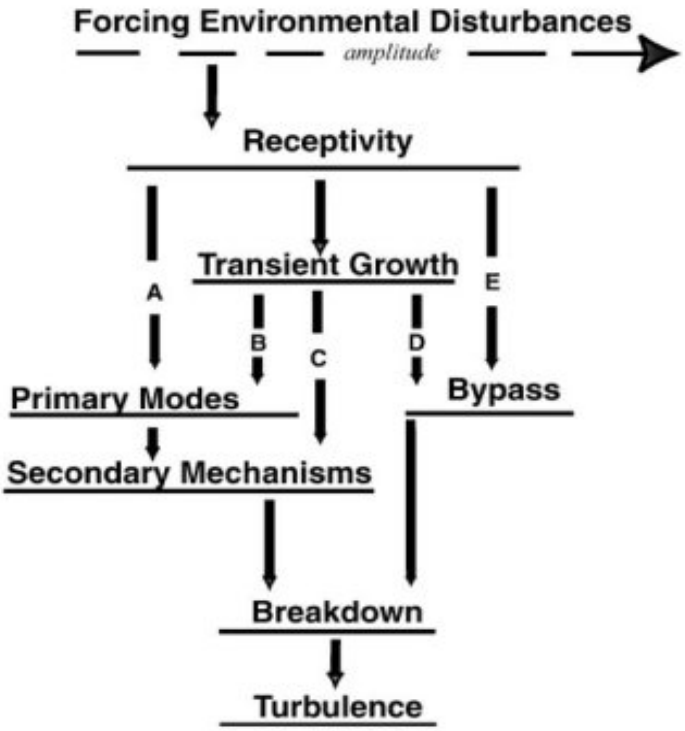

Figure 4: Transition to turbulence [13].

Figure 4 shows five different paths for transition:

1. **Natural Transition.**

   Natural transition occurs in weak disturbance environment. It is the path A in Figure 4. Breakdown is reached though linear process such as Tollmien Schilinting waves, Gortler or crossflow instabilities.

2. **Bypass Transition.**

   When the disturbance is sufficiently high, turbulent spots can form right away, skipping the growth of linear disturbances, as on path E.

3. **Intermediate Mechanisms**

   According to [15], additional mechanisms have been revealed apart from natural and bypass transition. These are the paths B, C and D.

The transition process in a quiet boundary-layer past a smooth surface,on a flat plate can be seen on Figure 5. Going downstream, the following areas can be observed [12]:

1. Stable laminar flow near the leading edge
2. Unstable two-dimensional Tollmien-Schlichting waves
3. Development of three-dimensional unstable waves and hairpin eddies

4. Cascading vortex breakdown into fully three-dimensional fluctuations
5. Formation of turbulent spots at locally intense fluctuations
6. Coalescence of spots into fully turbulent flow

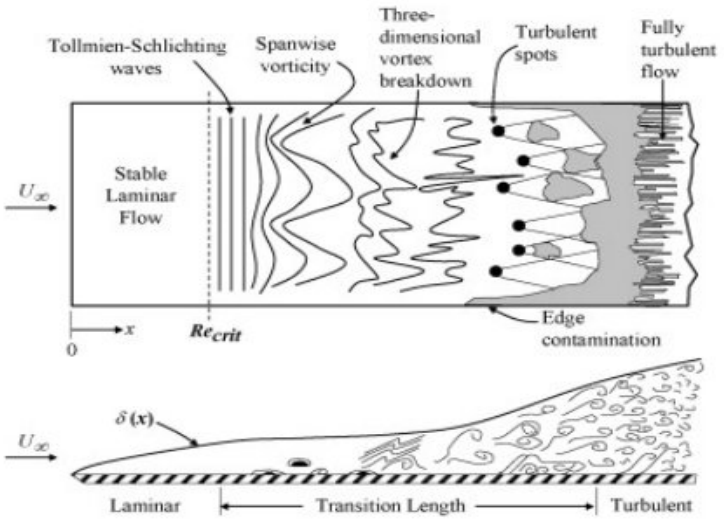

Figure 5: Flat plate transition [12].

The complexity of the phenomena related to the transition process presented in this chapter illustrates the reason why the physics of transition is still not entirely understood and is an active area of research. For this reason, it is argued that correlation-based models are more appropriate than the phenomenological models. The different factors affecting the transition process have to be studied in order to develop correlations, using which, the effects of these various factors will then be captured by the transition models.

3 Factors Affecting Transition

In this section, different factors affecting transition will be presented, including a sweep angle and roughness which are the topics of this work. Their effects and some techniques to predict them will be discussed.

3.1 Freestream Turbulence

A higher freestream turbulence intensity (Tu), will cause an earlier transition onset. At lower values of Tu, a natural transition occurs, while at higher, a bypass transition will take place. The freestream turbulence is a very important factor in determining transition as, according to experiment of Schubauer and Skramstad [16], at 0.35% turbulence level, the Reynolds number at which transition occurred dropped to half of its quiet value. Figure 6, shows how the turbulence intensity affects the momentum thickness Reynolds number at the beginning and end of the transition zone.

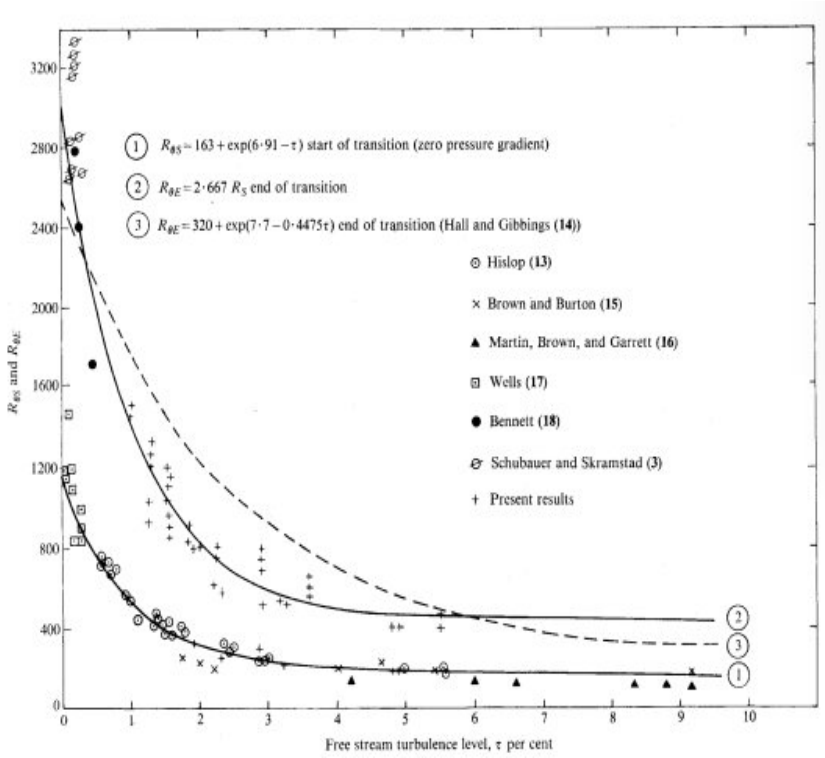

Figure 6: Variation of momentum thickness Reynolds number with freestream turbulence intensity [13].

There could be some other freestream disturbances that could unstabilize the laminar flow, such as acoustic noise, excited standing and travelling waves [12].

3.2 Streamwise Pressure Gradient

An adverse pressure gradient in the streamwise direction will destabilize the flow, while the favorable pressure gradient might cause relaminarization. This is illustrated

in Figure 7. In the figure, the momentum thickness Reynolds number is a function of the Thwaites parameter λ_θ, which describes the pressure gradient using the momentum thickness θ:

$$\lambda_\theta = \frac{\theta^2}{\nu}\frac{dU}{ds} \tag{9}$$

where s is the streamwise direction.

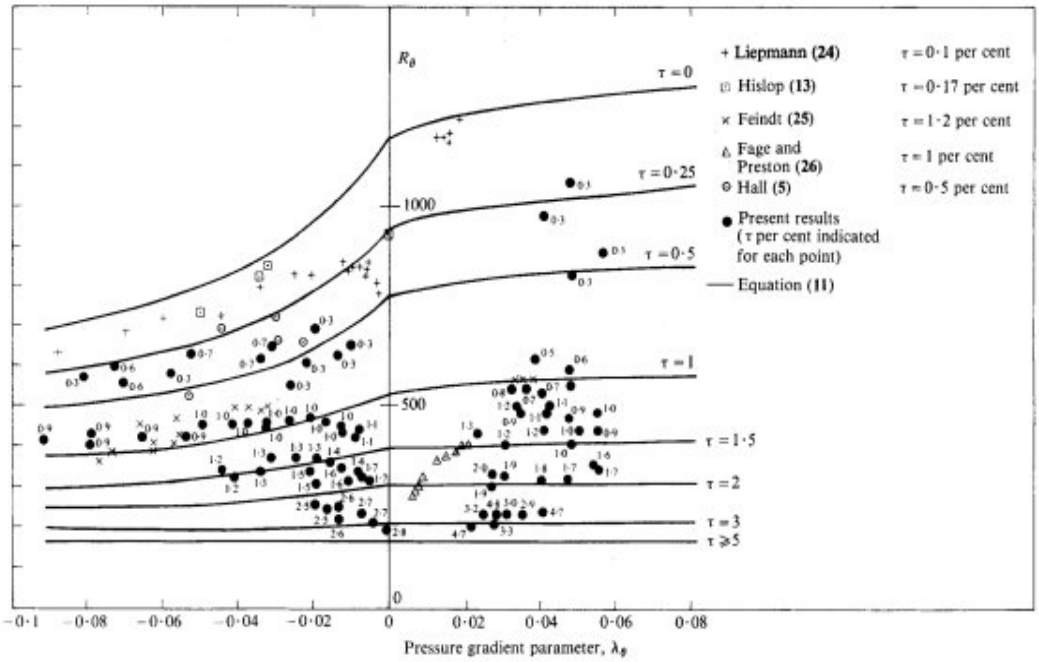

Figure 7: Effect of pressure gradient on transition onset on a flat plate [13].

Looking at Figure 7, it can be concluded that the adverse pressure gradient has a much stronger impact on accelerating transition, than the favorable pressure gradient on delaying it. While the pressure gradient is constant in the figure, in some other cases, such as airfoils, the pressure gradient tends to vary in the streamwise direction. The pressure gradient history becomes important in such cases.

3.3 Streamwise Surface Curvature

Concave and convex surfaces have an opposite effect on stability. The turbulence level entering a convex curve, is diminished due to the centrifugal acceleration. The boundary layer on an concave surface will become unstable due to the centrifugal forces (see Figure 8) [17]. The result is the formation of secondary flow in the form of counter-rotating vortices with axes parallel to the direction of the mean flow, called Görtler vortices, shown in Figure 9. At present, there are numerous methods to take the effects of curvature into account found in the literature, such as the empirical function proposed by Spalart and Shur [18].

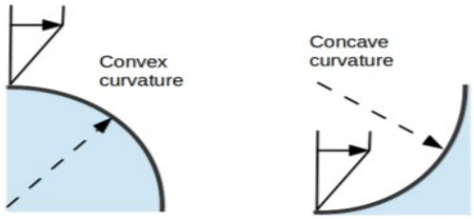

Figure 8: Concave and convex surfaces (Adapted from Durbin and Reif [17]).

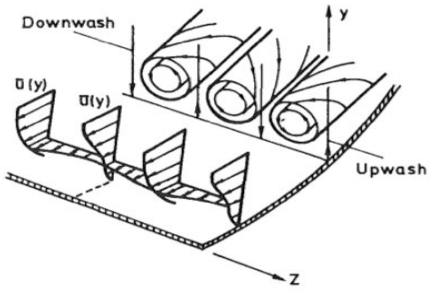

Figure 9: Görtler Vortices (Adapted from Finnis and Brown [19]).

3.4 Leading-edge Sweep

Crossflow transition can occur on swept wings before the streamwise Tollmien-Schlichting waves. This is due to the combination of sweep and pressure gradient. Considering 3D flows, the external velocity vector is not necessarily in the direction of the pressure gradients. Near the surfaces, the external streamlines are curved, which gives rise to crossflow. The pressure gradient does not vary in the wall-normal direction, whereas the streamwise velocity does and because of this, there is no balance between centripetal acceleration and pressure gradient. This will result in a secondary flow in the boundary layer, called crossflow, which is perpendicular to the direction of the inviscid streamline. The instability appears as co-rotating vortices whose axes are aligned to within a few degrees of the local invscid streamline [20].

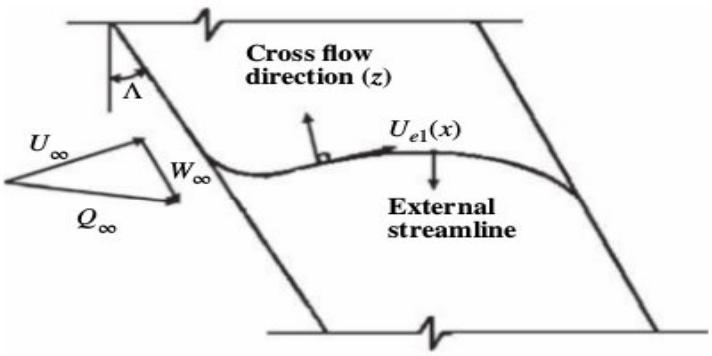

Figure 10: Inviscid streamlines on a swept wing [21].

The inviscid streamlines over the swept wing are shown in Figure 10. Close to the

leading edge of a swept wing, the surface and the streamlines are highly curved due to the combined effects of the pressure gradients and sweep angle, which turns the flow inboard [22]. The streamwise and crossflow components of the velocity inside a three-dimensional shear layer, are shown in Figure 11 [22]. The crossflow component has a maximum in the interior of the boundary layer and goes to zero at the wall and edge of the boundary layer.

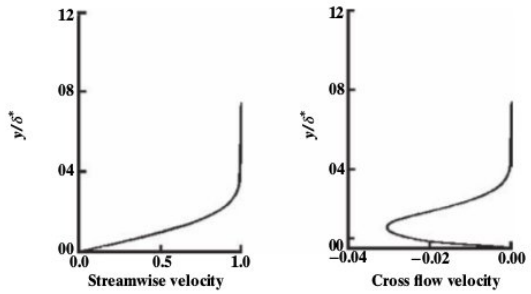

Figure 11: Streamwise and cross flow components of velocity [23].

3.5 Surface Roughness

The primary effects on the boundary layer flow are premature transition, thickening of fully turbulent boundary layer and increase of turbulent skin friction. In order to understand the effect of roughness, the height, shape and distribution should be considered [24].

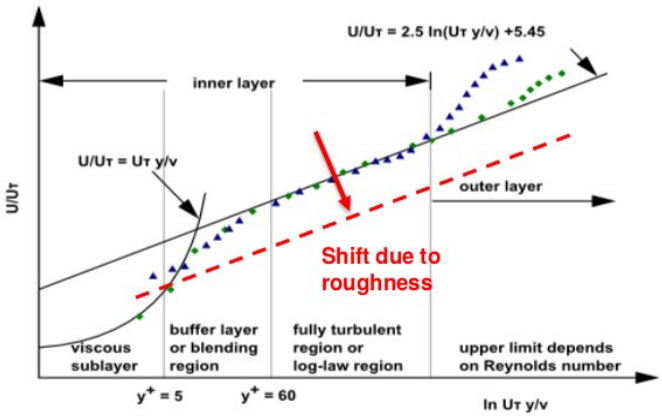

Figure 12: Effects of roughness on the turbulent boundary layer [24].

Roughness can have critical or subcritical behaviour. Roughness large enough that may immediately trigger transition are in the first group. Those with subcritical behaviour are difficult to predict, and will induce a shift in the transition location. Integrated effects and time histories need to be considered when modelling such roughness elements [24]. Roughness elements that have a height lower than the

viscous sublayer in general have a little effect on the transition process, since the disturbances are dissipated away due to high levels of viscous damping [6]. The effect of roughness on the turbulent boundary layer can be seen from Figure 12. There is a shift in the log-law.

Roughness can be classified broadly into three different subsets, two-dimensional roughness, isolated three dimensional roughness and distributed roughness [6]. The different types of roughness affect the transition process in a unique way. 2D roughness amplifies the naturally occuring Tollmien-Schlichting wave dominated transition process [6]. According to Gibbons, compressibility tends to diminish the effect of 2D roughness, and at a certain Mach number, it becomes negligible [25]. Isolated 3D roughness introduces structures like horseshoe and hairpin vortices, which have little effect on transition until height of the roughness reaches a point where transition location moves rapidly upstream. According to Refs. [26, 27], discrete 3D roughness elements can be used to delay crossflow transition. Finally, distributed roughness is more difficult to quantify, since one parameter is no longer enough to fully describe the roughness and its respective effects on transition. There have been some attempts to to correlate measurable parameters to an equivalent sand grain roughness heights [6].

4 Numerical Methodology

4.1 OpenFOAM Background

In this work, the OpenFOAM software is used [28]. OpenFOAM is an open source software used for continuum mechanics problems. It was developed at the Imperial College during the 1990's and was released under an open source license in 2004. From then until today, it has been constantly developing. Due to this, OpenFOAM has a wide range of models and solvers.

OpenFOAM is mainly a C++ library, used to create executables, which can be either solvers or utilities. Solvers are designed to solve a specific problem in continuum mechanics, while the utilities to manipulate data. It possess a pre- and post-processing environment apart from the CFD solver itself. The entire CFD process, from grid generation to post-processing can be done through the same C++ library. ParaView, however, the post-processing software provided with the regular OpenFOAM package is a stand-alone software.

OpenFOAM allows users to customize and extend its existing functionality. It does not require a license, and it can be executed in parallel without any licensing costs. This is very important for complex problems,where parallelization is required in order to achieve reasonable execution times for simulations. With some pre-requisite knowledge of underlying methods, physics and programming, the user can create new solvers and utilities.

4.2 Governing Equations

The governing equations in this work are based on the Navier-Stokes equations. These are a system of equations consisting of the conservation of mass, conservation of momentum and conservation of energy. The Navier-Stokes equations are based on the *continuum* assumption. This means that the representative length scale of the system should be much larger that the mean free path of the molecules, for this assumption to hold. The ratio of mean free path λ, and the representative length scale l, is called the Knudsen number, $\mathrm{Kn} = \frac{\lambda}{l}$. The Knudsen number is useful for determining whether statistical mechanics or the continuum mechanics formulation of fluid dynamics should be used. The Navier-Stokes equations are valid for $\mathrm{Kn} < 0.01$, which applies also in this work, as well as in technical applications in general. If $\mathrm{Kn} > 0.1$, the Navier-Stokes equations are not longer valid. In the intermediate region, $0.01 < \mathrm{Kn} < 0.1$, the Navier-Stokes equations can be used, but with special boundary conditions. The compressible Navier-Stokes equations in Einstein notation

are given by:

$$\frac{\partial \rho}{\partial t} + \frac{\partial \rho u_j}{\partial x_j} = 0 \tag{10}$$

$$\frac{\partial \rho}{\partial t} + \frac{\partial u_i u_j}{\partial x_j} = -\frac{\partial p}{\partial x_i} + \frac{\partial \sigma_{ij}}{\partial x_j} \tag{11}$$

$$\frac{\partial (\rho E)}{\partial t} + \frac{(\partial \rho E + p) u_j}{\partial x_j} = \frac{\partial (u_{ij} \sigma_{ij})}{\partial x_j} - \frac{\partial q_j}{\partial x_j}, \tag{12}$$

where ρ is the density, p is the pressure, u is the velocity in different directions, i, j, k, of the cartesian coordinate system and E is the total energy per mass unit. The stress tensor σ_{ij} is defined as

$$\sigma_{ij} = 2\mu S_{ij} - \frac{2}{3}\mu \delta_{ij} S_{kk} \tag{13}$$

where μ is the dynamic viscosity and δ the Kronecker delta, which is 1 if $i = j$ and 0 otherwise. The strain rate S is given by:

$$S_{ij} = \left(\frac{\partial u_j}{\partial x_i} + \frac{\partial u_i}{\partial x_j} \right)$$

In this work, the flow is assumed to be incompressible and isothermal, and so the equations become:

$$\frac{\partial u_i}{\partial x_i} = 0 \tag{14}$$

$$\frac{\partial u_i}{\partial t} + \frac{\partial u_i u_j}{\partial x_j} = \frac{\partial}{\partial x_j} \left(\nu \frac{\partial u_i}{\partial x_j} \right) - \frac{1}{\rho} \frac{\partial p}{\partial x_i} \tag{15}$$

where the energy equation has been removed, assuming incompressible and isothermal flow, and the first two, conservation mass and momentum are simplified. The density is constant, in space and time, and so the partial derivatives with respect to time and space are zero.

Turbulence modelling

As mentioned in the introduction, the RANS approach is much less computationally expensive than DNS and LES. The use of steady CFD methodologies (RANS) has advantages in that it can be used early in the design process because it is more efficient than the unsteady computation. In this approach, the governing equations are averaged in time, as seen in Figure 13. The effects of turbulence on the average flow field are modelled. The variables are separated into an average and fluctuating part. In the case of velocity:

$$u = \bar{u} + u' \tag{16}$$

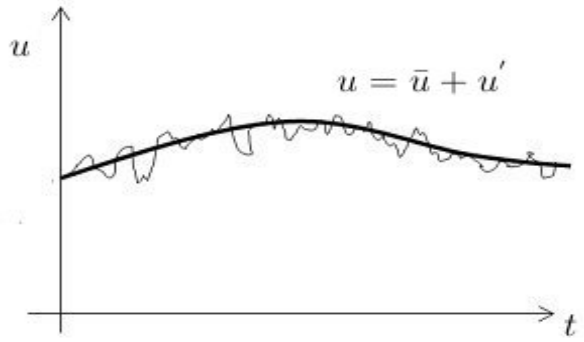

Figure 13: RANS averaging [9].

The time averaging of the velocity is defined as

$$\bar{u}(x) = \frac{1}{T}\int_0^T u(x,t)dt \tag{17}$$

Time T must be larger than the temporal fluctuations but smaller than temporal variations of interest. Applying the averaging process to the continuity equation:

$$\frac{\partial \overline{u}_i}{\partial x_i} = 0 \tag{18}$$

Since the continuity equation is linear, there are no extra terms after the averaging process. In the momentum equation, Eq. (15), the convection terms are nonlinear, and after averaging, extra terms are obtained, the Reynolds stress terms: $\overline{u_i' u_j'}$

$$\frac{\partial \overline{u}_i}{\partial t} + \frac{\partial \overline{u}_i \overline{u}_j}{\partial x_j} = \frac{\partial}{\partial x_j}\left(\nu \frac{\partial \overline{u}_i}{\partial x_j} - \overline{u_i' u_j'}\right) - \frac{1}{\rho}\frac{\partial \overline{p}}{\partial x_i} \tag{19}$$

The goal is to calculate the Reynolds stress from Eq. (19). There are three main categories of RANS-based turbulence models, and they are: Linear eddy viscosity models, nonlinear eddy viscosity models and the Reynolds stress model (RSM). In this work, a linear eddy viscosity model is used, which means that the reynolds stresses are approximated as:

$$-\overline{u_i' u_j'} = \nu_t\left(\frac{\partial u_i}{\partial x_j} + \frac{\partial u_j}{\partial x_i}\right) - \frac{2}{3}k\delta_{ij} \tag{20}$$

which is known as the Boussinesq hypothesis [29]. Assuming constant turbulent viscosity, the Reynolds stresses become:

$$\frac{\partial}{\partial x_j}(-\overline{u_i' u_j'}) = \frac{\partial}{\partial x_j}\left[\nu_t\left(\frac{\partial u_i}{\partial x_j} + \frac{\partial u_j}{\partial x_i}\right)\right] = \frac{\partial}{\partial x_j}\left(\nu_t \frac{\partial u_i}{\partial x_j}\right) \tag{21}$$

Inserting the relation into the momentum equation:

$$\frac{\partial \overline{u}_i}{\partial t} + \frac{\partial \overline{u}_i \overline{u}_j}{\partial x_j} = \frac{\partial}{\partial x_j}\left[(\nu + \nu_t)\frac{\partial \overline{u}_i}{\partial x_j}\right] - \frac{1}{\rho}\frac{\partial \overline{p}}{\partial x_i} \tag{22}$$

In order to solve the equation, it is necessary to obtain the turbulent viscosity ν_t. This can be done in different ways depending on the turbulence model that is chosen. In this work, a two-equation turbulence model is used, called the SST $k-\omega$ model. The model was first published by Menter in 1994 [30]. The basis was the $k-\omega$ model of Wilcox [31], and the standard $k-\epsilon$ closure [32]. The idea behind the model is to use the $k-\omega$ model in the sublayer of the boundary layer and switch to a transformed $k-\epsilon$ model elsewhere. The two transport equations are:

$$\frac{\partial}{\partial t}(\rho k) + \frac{\partial}{\partial x_j}(\rho u_j k) = P_k - D_k + \frac{\partial}{\partial x_j}\left[(\nu + \sigma_k \nu_k)\frac{\partial k}{\partial x_j}\right] \tag{23}$$

$$\frac{\partial}{\partial t}(\rho \omega) + \frac{\partial}{\partial x_j}(\rho u_j \omega) = \alpha \frac{P_k}{\nu_t} - D_\omega + Cd_\omega + \frac{\partial}{\partial x_j}\left[(\mu + \sigma_k \mu_t)\frac{\partial \omega}{\partial x_j}\right] \tag{24}$$

where k is the turbulence kinetic energy and ω is the specific turbulent dissipation rate. Cd_ω is the cross diffusion term, P represents the production terms, while D the destruction terms. The two models are blended using the F_1 function, which is applied as:

$$\phi = F_1\phi_1 + (1 - F_1)\phi_2 \tag{25}$$

where ϕ_1 and ϕ_2 are model coefficients from the two turbulence models $k-\omega$ and $k-\epsilon$, respectively. The model coefficients as well as the blending function F_1 can be found in Menter's publication [30]. After solving the two transport equations, the turbulent viscosity can be found from the relation:

$$\nu_T = \frac{k}{\omega} \tag{26}$$

4.3 Discretization of Equations

In order to solve the equations, they have have to be cast into a discrete form. There are various ways of doing this, and in this work the finite-volume method (FVM) is used. Other methods often used in CFD are finite differences and the finite element method.

Some advantages of the finite-volume method are that, similarly to the finite element method, it allows the use of arbitrary geometries, either structured or unstructured meshes. Another important feature, from the definition of the method, is that numerical fluxes are conserved locally, from one cell to the neighbour. This is an important feature when modelling problems where the flux is important, like in fluid mechanics [33]. In the finite-volume approach, the solution domain is divided into small control volumes. They are continuous and fill the domain completely without overlapping each other. The governing equations are integrated over these cells and the values are cell-averaged. Two such cells are presented in Figure 14.

The variables are stored at the centroids of the cells, which are located at points P and N, as shown in Figure 14. The cells are connected by faces f, which bound

the cells, and each face is owned by an adjecent cell while the other is called the neighbouring cell. $|\mathbf{S}_f|$ is the face area and $\mathbf{n}$ a unit normal vector, pointing towards the neighbour. The mesh in OpenFOAM is unstructured . The cells are not ordered in any way and are connected to each other only through faces, and not by any special indexing system, as in structured grids. [28]

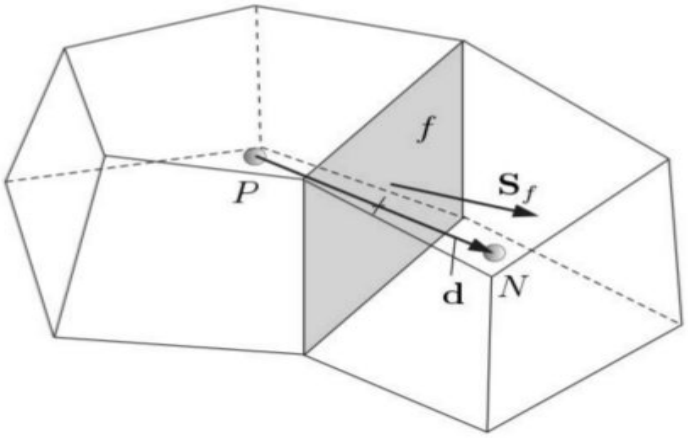

Figure 14: Finite-volume cells.

A general form of a transport equation is used in order to illustrate the discretization process.

$$\frac{\partial \phi}{\partial t} + \nabla \cdot (\mathbf{U}\phi) = \nabla \cdot (\alpha \nabla \phi) + \mathbf{q}_\phi \tag{27}$$

The equation is integrated over a control volume

$$\overbrace{\int_V \frac{\partial \phi}{\partial t} dV}^{\text{time derivative}} + \overbrace{\int_V \nabla \cdot (\mathbf{U}\phi) dV}^{\text{convection term}} = \overbrace{\int_V \nabla \cdot (\alpha \nabla \phi) dV}^{\text{diffusion term}} + \overbrace{\int_V \mathbf{q}_\phi}^{\text{source term}} \tag{28}$$

The time derivative and source terms are just multiplied by the cell volume. Different schemes for the time derivative can be chosen. If the implicit Euler method is used, the discretization would be:

$$\int_V \frac{\partial \phi}{\partial t} \approx \frac{(\phi V)^{n+1} - (\phi V)^n}{\Delta t} \tag{29}$$

The convection and diffusion terms are handled differently. The Gauss divergence theorem is applied on them, where the volume integral is transformed into a surface integral, and the convection term would become:

$$\int_V \nabla \cdot (\mathbf{U}\phi) dV = \int_S \phi U \cdot \mathbf{dS} \tag{30}$$

The surface integral is a sum over the discrete parts.

$$\int_V \nabla \cdot (\mathbf{U}\phi) dV = \int_S \phi \ \mathbf{U} \cdot dS \approx \sum_f \phi \mathbf{U} \cdot \mathbf{S}_f \tag{31}$$

Applying the method on the diffusion term, as in convection, the discrete form of the transport equation is obtained:

$$V_P \frac{\partial \phi}{\partial t} + \sum_f \phi \mathbf{U} \cdot \mathbf{S}_f = \sum_f (\alpha \nabla \phi) \cdot \mathbf{S}_f + V_P \mathbf{q}_\phi \tag{32}$$

After applying the Gauss divergence theorem, certain variables ($\mathbf{U}$, α, ϕ) are now expressed at the face of the cells. Since variables are stored at the centroids of the cells, they have to be interpolated. This can be done in different ways, using schemes such as the upwind scheme, central difference or high resolution schemes, which involve the limiter function. As examples, the upwind and central difference schemes will be presented. The upwind scheme is solution sensitive in that it determines the ϕ_f from the direction of the flow.

$$\phi_f = \begin{cases} \phi_P, & \mathbf{U} \cdot \mathbf{S}_f \geq 0 \\ \phi_N, & \mathbf{U} \cdot \mathbf{S}_f < 0 \end{cases} \tag{33}$$

The Taylor series expansion of a variable about a centroid P [34]:

$$\phi(x, y) = \phi_P + (\nabla \phi)_P \cdot \Delta \mathbf{r} + \mathcal{O}(|\Delta \mathbf{r}|^2) \tag{34}$$

if $\mathbf{r}$ is the distance vector from P to the face, the face value can then be expresses as follows

$$\phi_f = \phi_P + (\nabla \phi)_P \cdot \Delta \mathbf{r} \tag{35}$$

where by using the linear interpolation for the gradient term, the central difference scheme is obtained. The magnitude of the neglected terms is proportional to the square of the distance vector, and so it is second-order accurate. The upwind scheme is first-order accurate.

4.4 The Solution Algorithm

Since we are solving steady-state incompressible flows, the SIMPLE algorithm is used, first published by Patankar and Spalding [35]. It stands for Semi-Implicit method for Pressure-Linked Equations. For an unsteady flow, the PISO method, first proposed by Issa [36], tends to be used more often, however, in this work, no such a cases are simulated. SIMPLE and PISO fall into a category of the pressure correction methods. Although pressure correction methods were developed for incompressible flow, some variations for compressible flow also exist. The SIMPLE algorithm is implemented in OpenFOAM in the following manner [37]:

The momentum equation can be written as:

$$a_P \mathbf{U}_P = H(\mathbf{U}) - \nabla p \tag{36}$$

$\mathbf{U}_p$, the velocity vector of node P, is then expressed as (see Figure 14)

$$\mathbf{U}_p = \frac{H(\mathbf{U})}{a_P} - \frac{\nabla p}{a_P} \tag{37}$$

where $H(\mathbf{U})$ consists of two parts, a transport part which consists of matrix coefficients for all neighbours multiplied by the corresponding velocities, and a source part including all other source terms than the pressure gradient:

$$H(U) = -\sum a_N \mathbf{U}_N + \frac{\mathbf{U}^o}{\Delta t} \tag{38}$$

The discretized continuity equation is:

$$\nabla \cdot \mathbf{U} = \frac{1}{V_P} \sum_f \mathbf{S} \cdot \mathbf{U}_f = 0 \tag{39}$$

The face velocities are interpolated, similar to Eq. (37), as:

$$\mathbf{U}_f = \left(\frac{H(\mathbf{U})}{a_P} \right)_f - \frac{(\nabla p)_f}{(a_P)_f} \tag{40}$$

Eq. (40) is inserted in the in Eq. (39), and the pressure equation is obtained:

$$\nabla \cdot \left(\frac{1}{a_P} \nabla p \right) = \nabla \cdot \left(\frac{H(\mathbf{U})}{a_P} \right) = \sum_f \mathbf{S} \cdot \left(\frac{H(\mathbf{U})}{a_P} \right)_f \tag{41}$$

The SIMPLE algorithm is iterative and can be summarized as follows

1. Apply boundary conditions.
2. The discretized momentum equation is solved in order to find the intermediate velocity field. The pressure field from the previous iteration is used for the pressure terms. The equation is under-relaxed
3. The mass flux is calculated at the cells faces, which is then used for the pressure equations.
4. Solve the pressure equations and apply under-relaxation
5. The mass fluxes are corrected at the cell faces, using the results from the previous step.
6. The velocities are updated based on the new pressure field
7. The boundary conditions are updated
8. Repeat all till convergence.

The discretized governing equations form a system of algebraic equations. A general equation system can be written:

$$A\phi = Q \tag{42}$$

In CFD, such systems of equations are large and sparse, which means that only a few non-zero elements are present. Special algorithms can be applied to such systems. Used in this work are the preconditioned biconjugate gradient (PBiCG) and the generalized geometric-algebraic multi-grid (GAMG), described in Ref. [38]. PBiCG is used for all equations except the pressure equation. PBiCG is based on the conjugate gradient method. The idea behind this method is to reformulate the problem of solving the matrix equations as a minimization problem. The pressure equation is solved using GAMG. The solver starts with the matrix equation on the finest level, which is the computational grid. Then, step by step, the grid is coarsened until a certain level is reached and then it is refined again. The GAMG is a good choice for solving the pressure equation and is recommended by OpenFOAM documentation. It is an algebraic multi-grid solver. The idea behind such solvers is to use a coarse grid with fast solution times to smoothen out high frequency errors and to generate a starting solutions of the finer grid. This can be done by geometric coarsening of the grid (geometric multi-grid) or regardless of the geometry by applying the principles directly to the matrix (algebraic multi-grid). The iterations are also performed faster on the coarse level.

5 Local Correlation-Based Transition Model

5.1 Base Model

The transiton model used in this thesis is based on the paper by Menter and Langtry published in 2009 [39]. The original model was published in 2006 [2], however, some empirical correlations were missing from this document, which were finally published in the paper from 2009. Because of this, there have been different attempts to define these correlations, such as the one by Malan et al. [40,41]. The model is based on two transport equations, one for intermittency and another one for the transition onset Reynolds number. While in turbulence modelling the transport equation attempts to model the physics, the purpose of the transport equations in this model is only to form a framework for the implementation of the model into a general purpose CFD methods. The purpose of the transition onset momentum thickness Reynolds number is to capture the non-local influence of turbulence intensity and pressure gradient. The intermittency transport equation is then coupled with a turbulence model, in this case with the SST $k-\omega$ model, although it can be coupled with other turbulence models, such as the Spalart-Alamaras from the work of Medida [13].

5.1.1 Vorticity Reynolds number

The main idea behind the model is the use of the Van Driest and Blumer's vorticity Reynolds number concept [42] to link the transition onset Reynolds number from an empirical correlation and local boundary-layer quantities. This is the way that the model avoids the need to integrate the boundary-layer quantities, which is difficult to perform in 3D cases. The vorticity or alternatively the strain-rate Reynolds number used in this work is defined as

$$Re_v = \frac{\rho y^2}{\mu}\frac{\partial u}{\partial y} = \begin{cases} \approx \frac{\rho y^2}{\nu}\Omega, \\ \approx \frac{\rho y^2}{\nu}S, \end{cases} \tag{43}$$

where y is the distance from the nearest wall, Ω is the absolute value of the vorticity and S the absolute value of the strain rate. All quantities can easily be computed at each grid point in an unstructured, parallelized Navier-Stokes code.

In Figure 15, the scaled profile of the vorticity Reynolds number is shown. It is divided by 2.193 in order to have a maximum value of one inside the boundary layer. The momentum thickness Reynolds number is proportional to the maximum of the profile and is linked to the vorticity Reynolds number with the following relation:

$$Re_\theta = \frac{\max\left(Re_v\right)}{2.193} \tag{44}$$

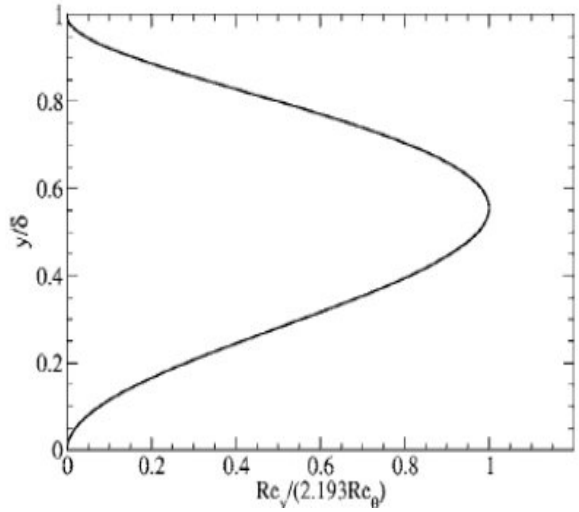

Figure 15: A scaled vorticity Reynolds number for a Blasius boundary layer

5.1.2 Intermittency

The transport equation for intermitency γ is developed in this section. The purpose is to solve the intermittency, which is then coupled with the turbulence model.

While in most applications, intermittency is defined as zero in the freestream and one as the fully turbulent state is reached, in this work, the freestream intermittency is set to one. This has a number of advantages, and it is particularly important in stagnation regions and near the boundary layer edge, where the original formulation interfered with the turbulence model. The transport equation for intermittency is given by:

$$\frac{\partial(\rho\gamma)}{\partial t} + \frac{\partial\rho(u_j\gamma)}{\partial x_j} = P_\gamma - E_\gamma + \frac{\partial}{\partial x_j}\left[\left(\mu + \frac{\mu_t}{\sigma_f}\right)\frac{\partial\gamma}{\partial x_j}\right] \tag{45}$$

where σ_f is the corresponding Schmidt number. The production source term is:

$$P_\gamma = F_{length} c_{a1} \rho S \left[\gamma F_{onset}\right]^{0.5} (1 - c_{e1}\gamma) \tag{46}$$

F_{lenght} controls the length of the transition region, while F_{onset} controls the transition onset location. The destruction/relaminarization source term is:

$$E_\gamma = c_{a2}\rho\Omega\gamma F_{turb}(c_{e2}\gamma - 1) \tag{47}$$

The following functions need to be defined:

$$Re_v = \frac{\rho y^2 S}{\mu} \tag{48}$$

$$F_{\text{onset}} = \max\left(F_{\text{onset2}} - F_{\text{onset3}}, 0\right) \tag{49}$$

$$F_{\text{onset1}} = \frac{Re_v}{2.913 \cdot Re_{\theta c}} \tag{50}$$

$$F_{\text{onset2}} = \min\left(\max\left(F_{onset1}, F_{onset1}^4\right), 2.0\right) \tag{51}$$

$$F_{\text{onset3}} = \max\left[1 - \left(\frac{R_T}{2.5}\right)^3, 0\right] \tag{52}$$

$$R_T = \frac{\rho k}{\mu \omega} \tag{53}$$

$Re_{\theta c}$ is the critical value for the Reynolds number, used to determine where the intermittency first starts to increase. The length of the transition zone F_{length} and $Re_{\theta c}$ are empirical correlations. F_{length} is obtained from [39]:

$$F_{\text{length}} = \begin{cases} [398.189 \cdot 10^{-1} + (-119.270 \cdot 10^{-4})\tilde{R}e_{\theta t} \\ + \quad (-132.567 \cdot 10^{-6})\tilde{R}e_{\theta t}^2], & \tilde{R}e_{\theta t} < 400 \\ [263.404 + (-123.939 \cdot 10^{-2})\tilde{R}_{\theta t} \\ + \quad (194.548 \cdot 10^{-5})\tilde{R}e_{\theta t}^2 + (-101.695 \cdot 10^{-8})\tilde{R}e_{\theta t}^3], & 400 \leq \tilde{R}e_{\theta t} \leq 596 \\ [0.5 - (\tilde{R}_{\theta t} - 596.0) \cdot 3.0 \cdot 10^{-4}], & 596 \leq \tilde{R}e_{\theta t} \leq 1200 \\ [0.3188], & 1200 \leq \tilde{R}e_{\theta t} \end{cases} \tag{54}$$

where $\tilde{R}e_{\theta t}$ is the local transition onset momentum thickness Reynolds number defined in the next subsection. F_{length} needs to be limited in the viscous sublayer. A sharp increase in y^+ inside the viscous sublayer, could cause a sharp increase in the skin friction, due to the dependence of F_{length} on $\tilde{R}e_{\theta t}$. This is corrected with the following equation:

$$F_{\text{length}} = F_{\text{length}}(1 - F_{\text{sublayer}}) + 40.0 \cdot F_{\text{sublayer}} \tag{55}$$

where the R_ω and F_{sublayer} are:

$$R_\omega = \frac{\rho y^2 \omega}{500\mu} \tag{56}$$

$$F_{\text{sublayer}} = e^{-(\frac{R_\omega}{0.4})^2} \tag{57}$$

The $Re_{\theta c}$ needed for the F_{onset1} is obtained from [39]:

$$Re_{\theta c} = \begin{cases} [\tilde{R}e_{\theta t} - (396.035 \cdot 10^{-2} + (-120.656 \cdot 10^{-4})\tilde{R}e_{\theta t} + (868.230 \cdot 10^{-6})\tilde{R}e_{\theta t}^2 \\ +(-696.506 \cdot 10^{-9})\tilde{R}e_{\theta t}^3 + (174.105 \cdot 10^{-12})\tilde{R}e_{\theta t}^4)], & \tilde{R}e_{\theta t} \leq 1870 \\ [\tilde{R}e_{\theta t} - (593.11 + (\tilde{R}e_{\theta t} - 1870.0) \cdot 0.482)], & \tilde{R}e_{\theta t} > 1870 \end{cases} \tag{58}$$

The model coefficients are:

$$c_{e1} = 1.0; \quad c_{a1} = 2.0 \quad c_{e2} = 5.0; \quad c_{a2} = 0.06; \quad \sigma_f = 1.0 \tag{59}$$

For the case where a flow separation takes place, additional modelling is required. Once a laminar boundary layer separates, the transition model would predict the turbulent reattachment too far downstream. It was proposed that the problem is due to the turbulent kinetic energy k growing too slowly in the separating shear layer to enable accurate reattachment [2]. To solve the problem, the intermittency is allowed to increase above the freestream value of one when separation occurs. The γ_{sep} variable was introduced:

$$\gamma_{\text{sep}} = \min \left\{ s_1 \max \left[0, \left(\frac{Re_v}{3.235 Re_{\theta c}} \right) - 1 \right] F_{\text{reattach}}, 2 \right\} F_{\theta t} \tag{60}$$

where F_{reattach} and s_1 are:

$$F_{\text{reattach}} = e^{-(\frac{R_T}{20})^4} \tag{61}$$

$$s_1 = 2 \tag{62}$$

The ratio of Re_v and $Re_{\theta c}$ is used as a measure of the size of laminar separation, since Re_v becomes much larger than the momentum thickness Reynolds number. When finally coupling the transport equations with the turbulence model, an effective intermittency γ_{eff} is defined as

$$\gamma_{eff} = \max(\gamma, \gamma_{\text{sep}}) \tag{63}$$

At the boundaries, the intermittency is set to $\gamma = 1$ at the inlet, and zero gradient is applied at the wall.

5.1.3 Transition momentum thickness Reynolds number

In order to obtain the value of $\tilde{Re}_{\theta t}$ needed for the intermitency equation, the transport equation for $\tilde{Re}_{\theta t}$ has to be solved. The experimental correlations relate the Reynolds number of transition to the turbulence intensity and other quantities in the freestream. However, the turbulence intensity can change strongly in the domain, therefore, setting one global quantity is not acceptable. The transport equation is used to pass the information about the freestream conditions into the boundary layer, as only local quantities can be used.

$$\frac{\partial(\rho \tilde{R}_{\theta t})}{\partial t} + \frac{\partial(\rho u_j \tilde{R}_{\theta t})}{\partial x_j} = P_{\theta t} + \frac{\partial}{\partial x_j} \left[\sigma_{\theta t} (\mu + \mu_t) \frac{\partial \tilde{R}_{\theta t}}{\partial x_j} \right] \tag{64}$$

where $\sigma_{\theta t}$ is a model coefficient. The source term $P_{\theta t}$ is created so that it forces $\tilde{R}_{\theta t}$ to be the same as the local value of $R_{\theta t}$ calculated by empirical correlation [39]:

$$P_{\theta t} = c_{\theta t} \frac{\rho}{t} (R_{\theta t} - \tilde{R}_{\theta t})(1.0 - F_{\theta t}) \tag{65}$$

The time scale $t = 500\mu/\rho U^2$ is defined for dimensional reasons. It was determined based on dimensional analysis with the main criteria being that it had to scale with the convective and diffusive terms in the transport equations. $F_{\theta t}$ is a blending function which is used to turn off the source term in the boundary layer and allow $\tilde{R}e_{\theta t}$ to diffuse in from the freestream. It is calculated from:

$$F_{\theta t} = \min\left\{ \max\left[F_{\text{wake}} \cdot e^{-(\frac{y}{\delta})^4}, 1.0 - \left(\frac{\gamma - 1/c_{e2}}{1.0 - 1/c_{e2}} \right)^2 \right], 1.0 \right\} \tag{66}$$

The following parameters need to be defined:

$$\theta_{\text{BL}} = \frac{\tilde{R}_{\theta t}\mu}{\rho U}; \quad \delta_{\text{BL}} = \frac{15}{2}\theta_{\text{BL}}; \quad \delta = \frac{50\Omega y}{U} \cdot \delta_{\text{BL}} \tag{67}$$

$$Re_\omega = \frac{\rho\omega y^2}{\mu}; \quad F_{\text{wake}} = e^{-(\frac{Re_\omega}{10^5})^2} \tag{68}$$

The model coefficient are:

$$c_{\theta t} = 0.03; \quad \sigma_{\theta t} = 2.0 \tag{69}$$

In order to calculate Re_θ, needed for the $\tilde{R}e_{\theta t}$ transport equation, empirical correlations are used. The correlation is based on two variables, the pressure gradient parameter λ_θ and Tu, the local turbulence intensity in percentages.

$$\lambda_\theta = \frac{\rho\theta_t^2}{\mu}\frac{dUs}{ds} \tag{70}$$

$$Tu = 100\frac{\sqrt{2k/3}}{U} \tag{71}$$

Term dU/ds is the acceleration along the streamwise direction and it can be computed in the following manner:

$$\frac{dU}{ds} = \frac{u}{U}\frac{dU}{dx} + \frac{v}{U}\frac{dU}{dy} + \frac{w}{U}\frac{dU}{dz} \tag{72}$$

where the velocity magnitude U is:

$$U = (u^2 + v^2 + w^2)^{\frac{1}{2}} \tag{73}$$

and the derivatives are found from:

$$\frac{dU}{dx} = \frac{1}{2U} \cdot \left[2u\frac{du}{dx} + 2v\frac{dv}{dx} + 2w\frac{dw}{dx} \right] \tag{74}$$

$$\frac{dU}{dy} = \frac{1}{2U} \cdot \left[2u\frac{du}{dy} + 2v\frac{dv}{dy} + 2w\frac{dw}{dy} \right] \tag{75}$$

$$\frac{dU}{dz} = \frac{1}{2U} \cdot \left[2u\frac{du}{dz} + 2v\frac{dv}{dz} + 2w\frac{dw}{dz} \right] \tag{76}$$

$$\tag{77}$$

The empirical correlations are computed from [39]:

$$Re_{\theta t} = \left[1173.51 - 589.428Tu + \frac{0.2196}{Tu^2}\right] F(\lambda_\theta), \qquad Tu \leq 1.3 \tag{78}$$

$$Re_{\theta t} = 331.50[Tu - 0.5658]^{-0.671} F(\lambda\theta), \qquad Tu > 1.3 \tag{79}$$

$$F(\lambda_\theta) = 1 - [-12.986\lambda_\theta - 123.66\lambda^2 - 405.689\lambda_\theta^3]e^{-[\frac{Tu}{1.5}]^{1.5}} \qquad \lambda_\theta \leq 0 \tag{80}$$

$$F(\lambda_\theta) = 1 + 0.275\Big[1 - e^{[-35.0\lambda_\theta]}\Big]e^{\frac{-Tu}{0.5}} \qquad \lambda_\theta > 0 \tag{81}$$

The following parameters are limited for robustness:

$$-0.1 \leq \lambda_\theta \leq 0.1 \qquad Tu \geq 0.027\% \qquad Re_{\theta t} \geq 20 \tag{82}$$

At the inlet, the boundary condition is solved from $Re_{\theta t}$ empirical correlations. On the walls, the zero normal flux is used.

5.1.4 Coupling with the turbulence model

In this work, the transition model is coupled with the SST $k-\omega$ turbulence model. The original form is given by Eqs. (23) and (24). The model is modified in order to incorporate the transition model, and is given by:

$$\frac{\partial}{\partial t}(\rho k) + \frac{\partial}{\partial x_j}(\rho u_j k) = \tilde{P}_k - \tilde{D}_k + \frac{\partial}{\partial x_j}\left[(\nu + \sigma_k \nu_k)\frac{\partial k}{\partial x_j}\right] \tag{83}$$

$$\frac{\partial}{\partial t}(\rho \omega) + \frac{\partial}{\partial x_j}(\rho u_j \omega) = \alpha\frac{P_k}{\nu_t} - D_\omega + Cd_\omega + \frac{\partial}{\partial x_j}\left[(\mu + \sigma_k \mu_t)\frac{\partial \omega}{\partial x_j}\right] \tag{84}$$

The modified production and destruction terms are:

$$\tilde{P}_k = \gamma_{eff} P_k \tag{85}$$

$$\tilde{D}_k = \min\left(\max\left(\gamma_{eff}, 0.1\right), 1.0\right) D_k \tag{86}$$

Where P_k and D_k are the production and destruction terms from the original equation. The modified blending function and related variables are:

$$F_1 = \max\left(F_{1orig}, F_3\right) \tag{87}$$

$$R_y = \frac{\rho y\sqrt{k}}{\mu} \tag{88}$$

$$F_3 = e^{-[\frac{R_y}{120}]^8} \tag{89}$$

It was found that the blending function can change from 1.0 to 0.0 in the middle of the laminar boundary layer [2]. This is undesirable, and so it is fixed to be equal to 1.0 always in the laminar boundary layer.

5.2 Model Extension

In this section, the model extensions for the roughness- and crossflow-induced transition will be presented. The implementation in OpenFOAM is shown in Appendix A.

5.2.1 Roughness effects

The roughness extension is based on the work by Langel et al. [6], and is presented in this section. In order to account for the effects of an additional transport equation is introduced into the transition model. The transport equations is for a variable called *Roughness Amplification*, A_r and is given:

$$\frac{\partial(\rho A_r)}{\partial t} + \frac{\partial(\rho u_j Ar)}{\partial x_j} = \frac{\partial}{\partial x_j}\left[\sigma_{ar}(\mu + \mu_t)\frac{\partial Ar}{\partial x_j}\right] \tag{90}$$

where σ_{ar} is a model constant. A_r is transported by convection and diffusion through the flow field, and this behaviour enables the flow history effects to be taken into account. The roughness-induced amplification of disturbances can show a large lag between the amplification location and the position where the boundary layer reacts to the distortion. Such a phenomenon is a flow history effect, and can be accounted for by transport equations. In order to link Ar to the original transition model, the source term of the $Re_{\theta t}$ transport equation, Eq. (64), is modified:

$$P_{\theta t,mod} = c_{\theta t}\frac{\rho}{t}\Big[(Re_{\theta t} - Re_{\theta t})(1 - F_{\theta t}) - F_{Ar}\Big] \tag{91}$$

F_{Ar} is determined according to [6] as

$$F_{Ar} = \begin{cases} c_{Ar2} \cdot (A_r)^3, & A_R < C_{Ar} \\ c_{Ar3}(A_r - C_{Ar}) + c_{Ar2}C_{Ar}^3, & A_r \geq C_{Ar} \end{cases} \tag{92}$$

The boundary conditions for the ω-equation are changed from the original SST model to

$$\omega_{wall} = 10\frac{6\nu}{\beta(\Delta y)^2}, \quad \text{where} \quad \beta = 0.09 \tag{93}$$

where Δy represents the normal distance from the wall to the nearest grid point. The modification is done according to the following relationships

$$\omega_{rough} = \frac{\mu_\tau^2 S_r}{\nu} \quad \text{with} \quad \mu_\tau = \sqrt{\frac{\tau_\omega}{\rho_\omega}} \tag{94}$$

Variable S_r is dependent on the dimensionless surface roughness k^+ as

$$S_r = \left(\frac{50}{k^+}\right)^2 \quad \text{if} \quad k^+ \leq 25 \tag{95}$$

$$S_r = \frac{100}{k^+} \quad \text{if} \quad k^+ > 25 \tag{96}$$

where k^+ is defined as:

$$k^+ = \sqrt{\frac{\tau_w}{\rho_w}} \frac{k_s}{\nu} \tag{97}$$

The boundary condition for A_r is given by

$$A_r|_{wall} = c_{A_r1} k^+ \tag{98}$$

and the model coefficients are:

$$c_{Ar1} = 8.0 \quad c_{Ar1} = 0.0005 \quad c_{Ar1} = 2.0 \quad c_{Ar1} = 10.0 \tag{99}$$

5.2.2 Crossflow effects

The crossflow extension is based on the work by Müller et al. [7]. There are different attempts to include the crossflow effects into the base model, such as the one by Seyfert and Krumbein [43], which has the deficiency that it requires the sweep angle to be given as a boundary condition. The model by Watanabe et al. [44] lacks the ability to capture the flow history effects effects. To the author's knowledge, the model by Müller et al. is the most recent attempt to include the crossflow effects into the local-correlation based transition model. According to the publication, in order to add the crossflow effects to the transition model, the source term for $Re_{\theta t}$ is changed. The following is added to Eq. (64):

$$P_{CF} = -\min\Big(\max\left[0, \left(\frac{\rho}{1000 \cdot t} \cdot \left(\frac{Re_H}{6}\right)^{c_1} \cdot (Re_\Omega)^{c_2} \cdot \left(\frac{12\theta}{y}\right)^{c_3} - c_4\right) \cdot c_5\right], c_6\Big) \tag{100}$$

P_{CF} is always negative, because lowering $Re_{\theta t}$ triggers transition. Re_H is the Reynolds number based on the local helicity, and is defined as

$$Re_H = \frac{\theta}{\nu}\sqrt{\theta H} \tag{101}$$

where H, the helicity, is defined as

$$H = |\boldsymbol{U} \cdot \boldsymbol{\omega}| \tag{102}$$

where $\boldsymbol{\omega}$ is the vorticity and $\boldsymbol{U}$ the velocity vector. Helicity is at maximum when the flow is rotating around the velocity vector. Exactly this is observed in the area of crossflow instabilities in an accelerated boundary layer. The Reynolds number based on vorticity is defined:

$$Re_\Omega = \frac{\rho y^2}{\mu}\Omega \tag{103}$$

Similar to the original formulation of Langtry and Menter, though it is based on the magnitude of the vorticity tensor Ω. Term $\frac{\theta}{y}$ is used for correction. It was found that Re_H based on θ works well only in a few cases. Better results were obtained by using y instead on some other cases. The term was added to vary the two characteristic length scales independent of each other.

Unfortunately θ was not defined in the publications, however, in a previous paper, by the same author, it was defined as

$$\theta = \frac{Re_v \mu}{2.193 U \rho} \tag{104}$$

The coefficient used in the model are:

$$c_1 = 0.548, \quad c_2 = 0.1912, \quad c_3 = -0.298, \quad c_4 = 0.0, \quad c_5 = 60.0, \quad c_6 = 1666.5 \tag{105}$$

The constants show the strong influence of the helicity Reynolds number, since it is weighted by c_1, and $c_1 > c_2 > c_3$.

6 Validation of Roughness-induced Transition

The roughness extension is tested against three flat plate cases: a zero-pressure gradient, a favorable-pressure gradient and an adverse-pressure gradient. The results are compared with those from Langel and Chow publication [6]. Since the transition model is sensitive to convection schemes [2], it is important to emphasize which schemes are used. The scheme used for the convection terms is the linear-upwind method in all cases, which has a second-order accuracy.

The grids were created following the guidelines by Langtry [2], since the transition model showed great dependencies on the grid. Following flat plate tests, it was found by Langtry that when y^+ is between 0.001 and 1, the grid has a very little effect on the solution. Once it is increased above 8, the point of transition onset starts to move upstream. Below 0.001, the point of transition onset moves downstream. The wall normal expansion ratio also has an effect on the solution. For values of 1.2 and 1.4, the transition onset point moved upstream in the study. Finally, the streamwise grid refinement is important to consider, since the grid has to be well resolved, otherwise the transition point can move upstream. Having these results in mind, the grids were tested until grid independent solutions were found. For all test cases, the grid was adjusted, so that the y^+ is varied between $0.2 < y^+ < 1$ along the plate.

According to the publication by Langel and Chow [6], all three simulations were done with Ma = 0.1. This was applied also in this thesis, except in the adverse pressure gradient, because the point of transition could not move further downstream to the value given in the publication, by lowering the turbulence intensity. To match the results, the turbulence intensity had to be changed somewhat for all cases. The reason could be differences in the implementation of the transition model in OpenFOAM and in OVERFLOW-2 [6], which was used by Langel and Chow. In their publication, the freestream intensity had to be adjusted for the favorable pressure gradient case, to match the transition onset with another publication [45], and the reasoning was that the difference in the implementation could be the issue. The eddy viscosity ratio $\mu_\tau/\mu = 9$ was applied to all cases, like in Langtry's thesis [2], for a case with a similar turbulence intensity. The roughness height was selected according to the equivalent sand grain roughness height Reynolds number Re_{ks}, defined as:

$$Re_{ks} = \frac{u_\infty k_s}{\nu} \tag{106}$$

where u_∞ is the freestream velocity and k_s is the equivalent sand grain roughness height. The two pressure gradient cases were simulated by applying the slip boundary condition to the top boundary, and changing its geometry according to the formula:

$$r(x) = \sqrt{\frac{r_0^2}{\sqrt{1 - PG}}} \quad \text{with} \quad PG = \frac{p_1(x) - p_0}{q_0} \tag{107}$$

where p_0 and q_0, are the static and the dynamic pressures at the inlet, respectively, and p_1 is the static pressure along the plate. The distance from the flat plate to the upper wall at inlet r_0, is set to 0.1495. PG is set to:

$$\frac{p_1(x) - p_0}{q_0} = \pm 4.0x \tag{108}$$

depending on whether it is an adverse or a favorable pressure gradient.

6.1 Zero Pressure Gradient

6.1.1 Case setup

The mesh used for the zero pressure gradient is shown in Figure 16 for different Re_{ks}. The symmetry boundary condition is used for the top boundary as well as for the surface in front of the plate. The boundary condition types used are the same as those from Langtry's thesis [2], for a zero pressure gradient case.

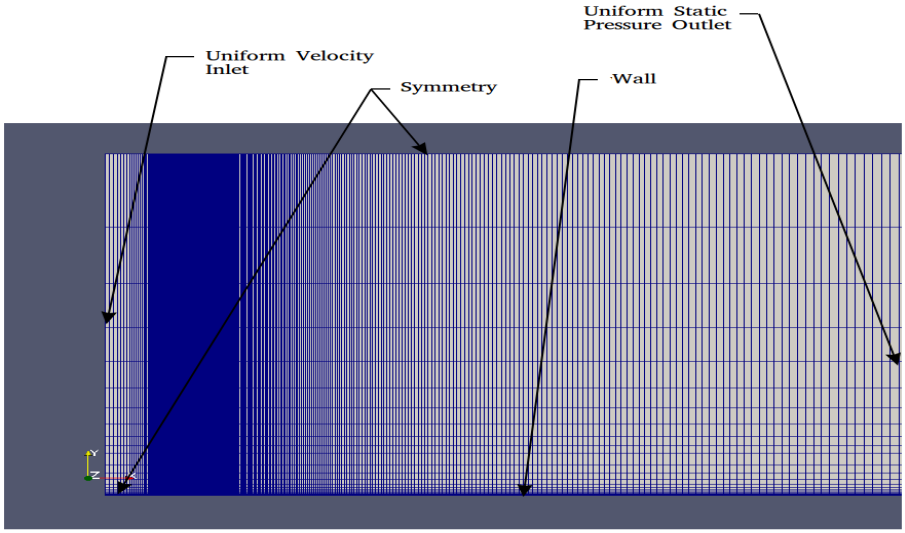

Figure 16: Zero pressure gradient mesh

In order to match the transition onset point, the turbulence level of 1.01% was set at the inlet. The turbulence intensity used by Langel and Chow [6] was 0.91%.

6.1.2 Results

The results are given in Figure 17 for different values of Re_{ks}. Compared to the results of Langel and Chow [6] in Figure 18, the transition onset is predicted far too upstream. The value for the wall shear stress seems to be slightly higher. In Figure 19, the results without the corrected ω wall boundary conditions, Eq. (95) and (96), are shown. The new boundary conditions seems to show a correct behavior by increasing the value of the wall shear stress much closer to the values of Langel and Chow's results. This behavior is observed for the other cases as well in Figures 23 and 27.

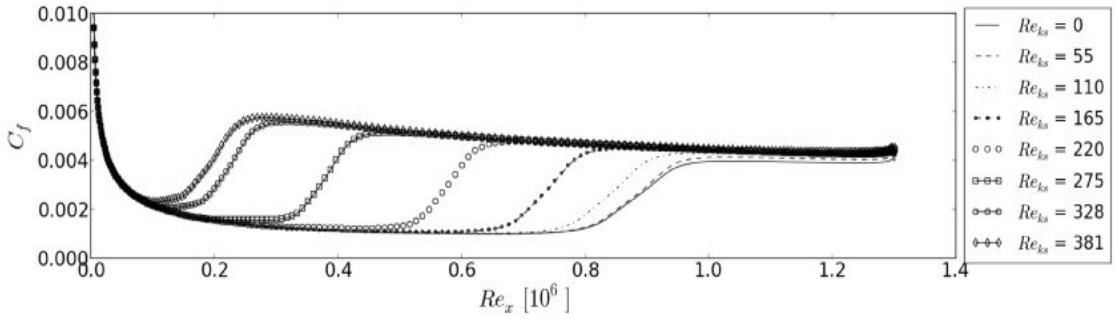

Figure 17: Zero-pressure gradient results from Langel and Chow [6].

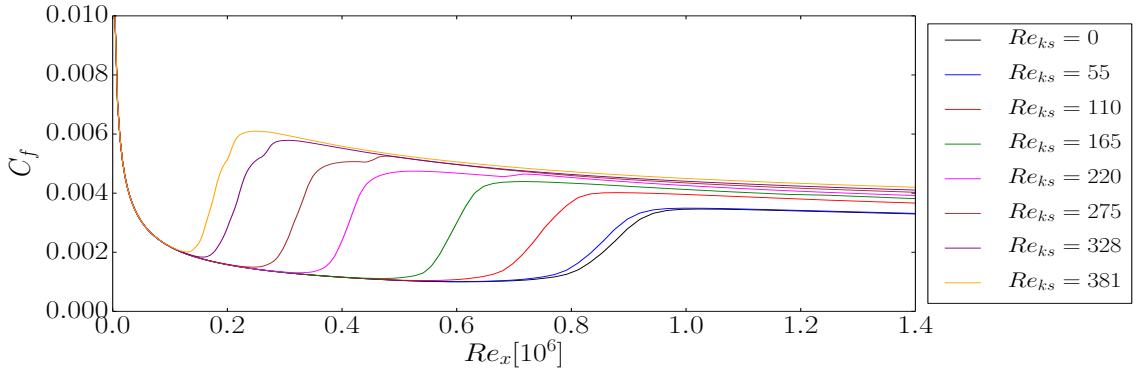

Figure 18: Zero pressure gradient results.

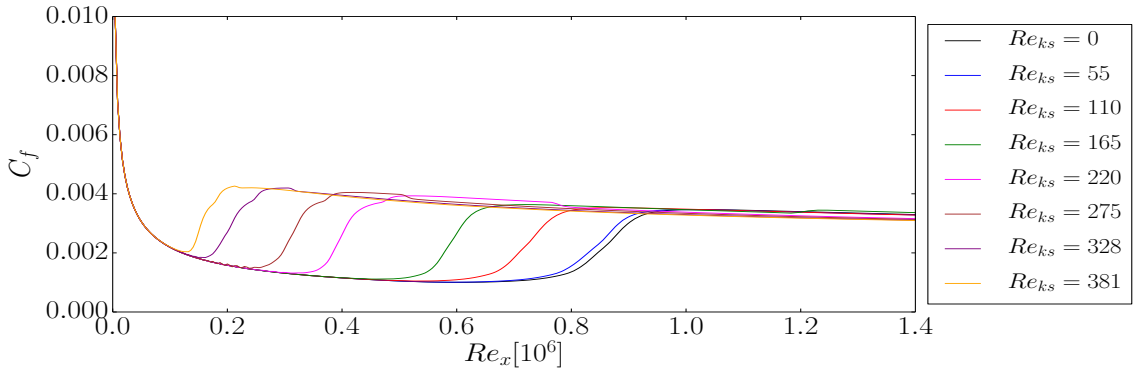

Figure 19: Results without the corrected boundary conditions for ω.

6.2 Favorable Pressure Gradient

6.2.1 Case setup

The mesh used for the favorable pressure gradient case, is presented in Figure 20. As in the case of a zero-pressure gradient, the boundary condition types were the same as those from Langtry's thesis, for the case of pressure gradients. Instead of a symmetry boundary condition, a slip boundary condition was applied at the top. The same approach is used for the case of the adverse-pressure gradient, in Figure 24. At the inlet, the turbulence intensity was set to 1.15%.

6.2.2 Results

From the results, it can be seen that again, the transition onset is predicted too upstream, although better than in the case of zero-pressure gradient. The values for the wall shear stress appear too high in this case. In the publications of Langel and Chow, a high freestream turbulence intensity had to be applied, much higher than in this thesis, 2.1 %, which could be the reason for such a difference in the shear stress values.

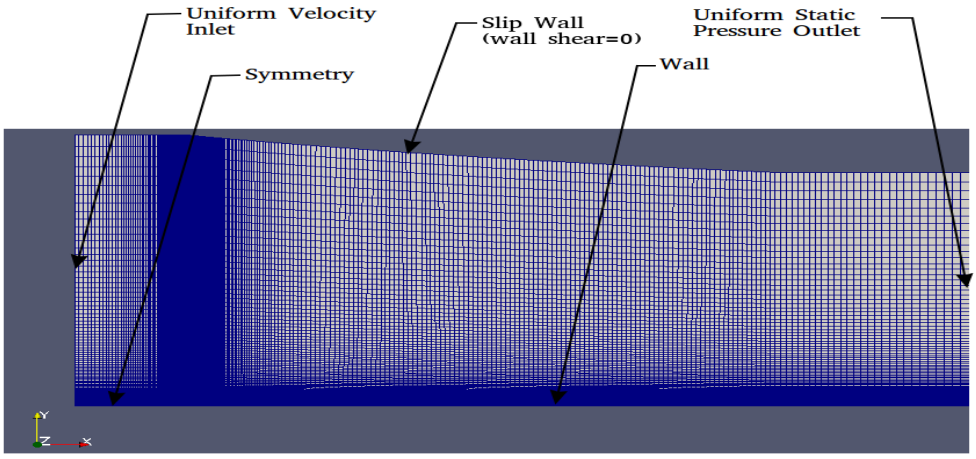

Figure 20: Favorable pressure gradient mesh.

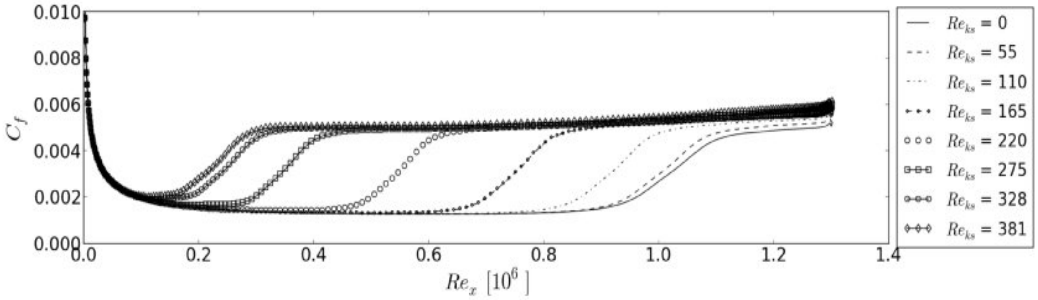

Figure 21: Favorable-pressure gradient results from Langel and Chow [6].

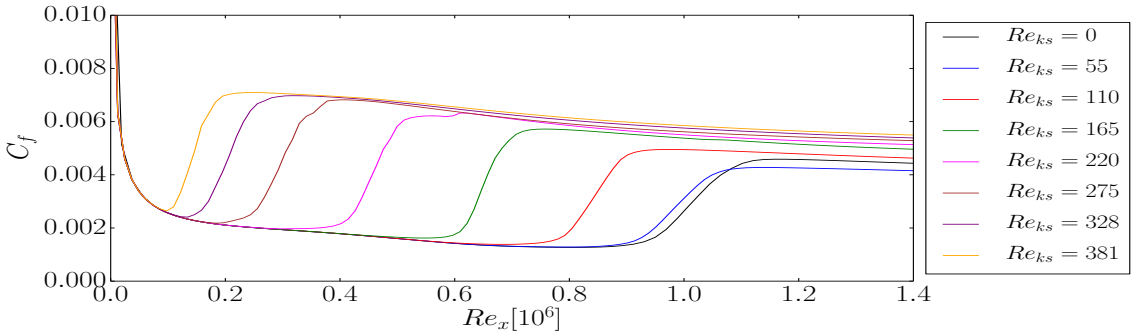

Figure 22: Favorable pressure gradient results.

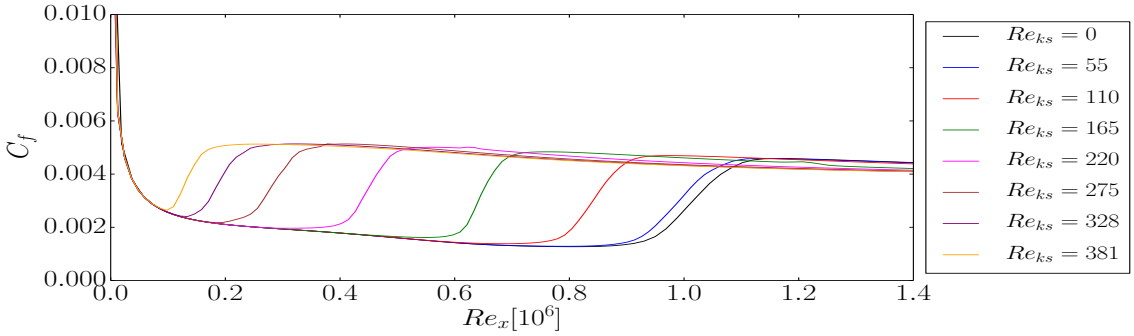

Figure 23: Results without the corrected boundary conditions for ω.

6.3 Adverse Pressure Gradient

6.3.1 Case setup

The mesh for the case of adverse-pressure gradient is shown in Figure 24. The turbulence intensity was set to be 1.02%, and the velocity to $u_\infty = 100\,\mathrm{m/s}$ at the inlet, instead of Ma=0.1, as in the previous cases. The equivalent sand grain roughness heights were adjusted according to the equivalent sand grain roughness height Reynolds numbers Re_{ks}. This was done in order to move the transition onset point, for the case without roughness, to the one from the publication of Langel and Chow [6], as explained at the beginning of this chapter. Lowering of the turbulence intensity had no effect after a certain point, so the speed was changed, and the roughness heights were adjusted according to Eq. (106).

6.3.2 Results

For this case, it seems that the computed results and those of Langel and Chow [6], are much closer together, than in the previous computations. The problem is that the wall shear stress are predicted as too low. The velocity in this case is different than from the publication. However, it was also compared with the work of Dassler et al. [45], where the velocity was also 100 m/s, and the wall shear stress were again lower.

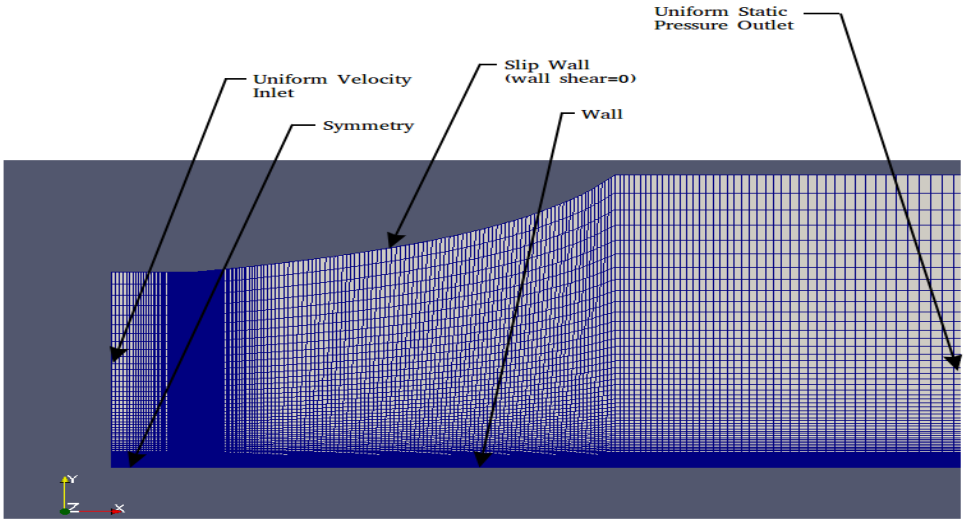

Figure 24: Adverse pressure gradient mesh.

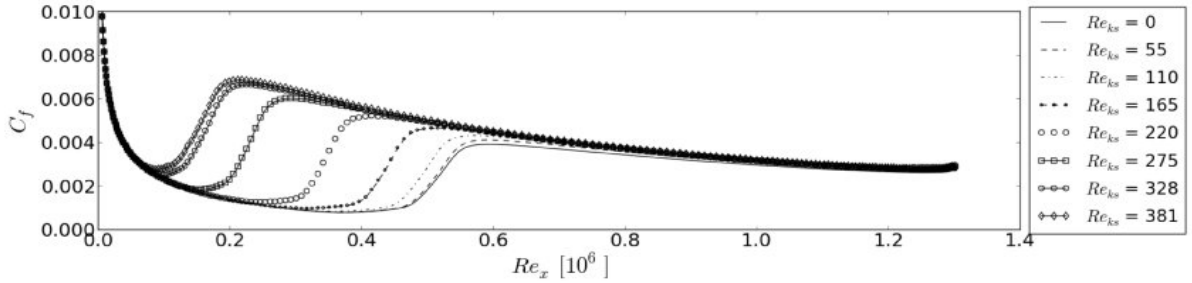

Figure 25: Adverse-pressure gradient results from Langel and Chow [6].

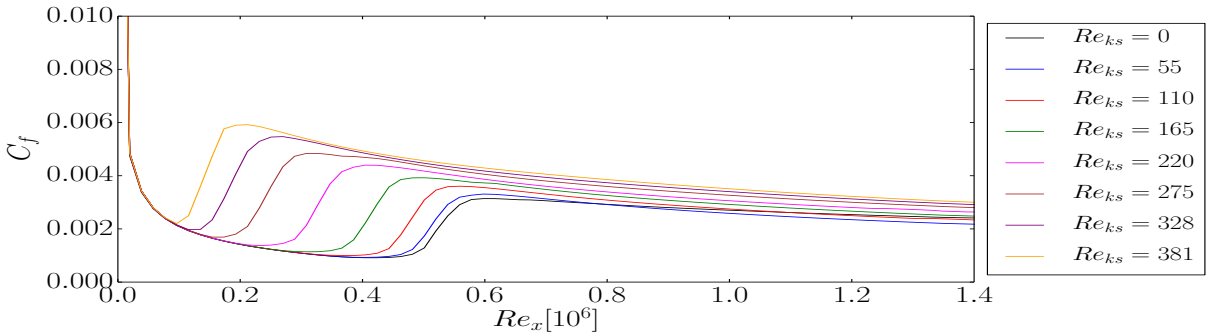

Figure 26: Adverse pressure gradient results.

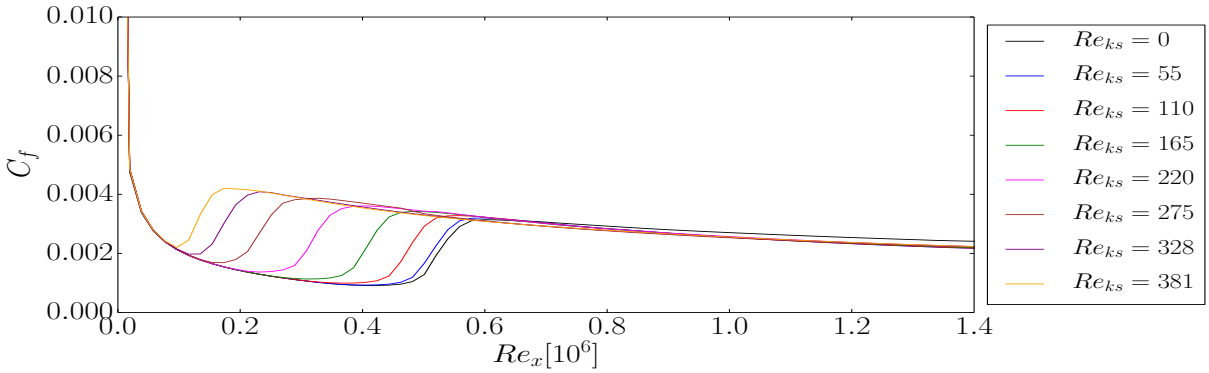

Figure 27: Results without the corrected boundary conditions for ω.

6.4 General Conclusions

Comparing the three cases, it seems that the zero-pressure gradient case yields to the worst results in terms of the transiton onset prediction. The favorable-pressure gradient case shows better agreement, while the adverse shows the best. Looking at the wall shear stress, the zero-pressure gradient case gives the best results, while the favorable gives the worst. The model shows a lot of sensitivity to turbulence freestream conditions. The decay of freestream turbulence variables, k and ω were limited in the simulations. Without the limitation, higher values of Tu had to be applied in order to get the same transition onset as in the publication [6], for zero roughness. After applying the roughness, the results changed quite a bit, for the zero-pressure gradient case especially. Using the higher Tu, the lower roughness heights were better predicted, while for the limited turbulence decay case, with a lower Tu, higher roughness height cases were closer in agreement. This change in Tu also had an effect on the wall shear stress, maybe due to ω, which could explain why the favorable-pressure gradient case was so different from the publication. Using different values of the eddy viscosity ratio, the freestream ω was varied, and above a certain point, the wall shear stress decreases dramatically, without changing the transition onset point. The new wall boundary condition has a similar effect, in that a lower ω at the wall increased the wall shear stress. The zero-pressure gradient case also showed a greater sensitivity to the y^+ than the other two.

Two implementations of the transition model were used for these cases. One was obtained from The Chalmers University of Technology [46], while the other, was downloaded from Ref. [47], and is the more validated model, however, neither implementation is officially part of OpenFOAM. Even though both models were able to predict flat plate cases from Langtry's publication [2] and some airfoil cases with the same results, once the roughness extension was applied, they behaved very differently. This shows that the implementation affects the behavior of the model significantly. This was observed after experimenting with the two implementations, and limiting certain variables at different locations. The difference in the implementation could be a reason why the results are so different from the publication. It was observed

that in the case of the zero-pressure gradient, without the surface roughness, the effect of y^+ is higher that what is discussed by Langtry in his thesis, under best practice guidelines. This could point that the transition model should be further validated and corrected. Also, the turbulence decay was limited in a different way in the publication. In this thesis, the variables were just limited with max(), by not allowing the variables to decrease below the freestream values. In the publication, the ω transport equation was modified, and this changes the behavior of the model, according to the publication. Unfortunately, this modification was not published in detail. This could also explain the difference in the results, considering the sensitivity of the model. The adverse pressure gradient case resulted in the best results, but according to Section 3.2, the adverse pressure gradient has a stronger impact on accelerating transition than favorable-pressure gradient, so the effects of freesteram turbulence could be weaker in this case.

7 Crossflow-induced Transition Validation

7.1 Case Setup

In order to validate the crossflow-induced transition model, the Onera M6 wing case was used. The flow is incompressible and the case is based on the paper by Schmitt et al. [48], where the velocity and Reynolds number are given as Ma = 0.262 and $\mathrm{Re} = 3.5 \cdot 10^6$, respectively. The mesh was done in blockMesh, which was used in the work and provided by the author of Ref. [49]. The mesh was further refined in order to follow the guidelines set by Langtry [2]. There are 12 172 350 cells in the domain for the $\alpha = 0°$ and $\alpha = 5°$ angle of attack cases and 13 133 325 for $\alpha = 15°$. The 3D mesh is shown in Figure 28. A close up on the wing surface shows the grid density in Figure 29. For clarity, the mesh is twice as coarse as the one used in the simulation, in both x- and y-direction. The mesh in the z-direction was also refined, in order to lower the y^+ value. The convection scheme used is the Gauss limitedLinear 1, which is the limited linear scheme, in this case, the Sweby limiter [50] is used, which is applied with option "1" [51]. When the scheme from the roughness simulations was applied, the transition could not be observed, only oscillations of the wall shear stress on the surface of the wing. The turbulence intensity and turbulent viscosity ratio at farfield were set to $Tu_{ff} = 3\%$ and $(\mu_\tau/\mu)_{ff} = 40$, respectively, following the guidelines from Krumbein and Grabe [52].

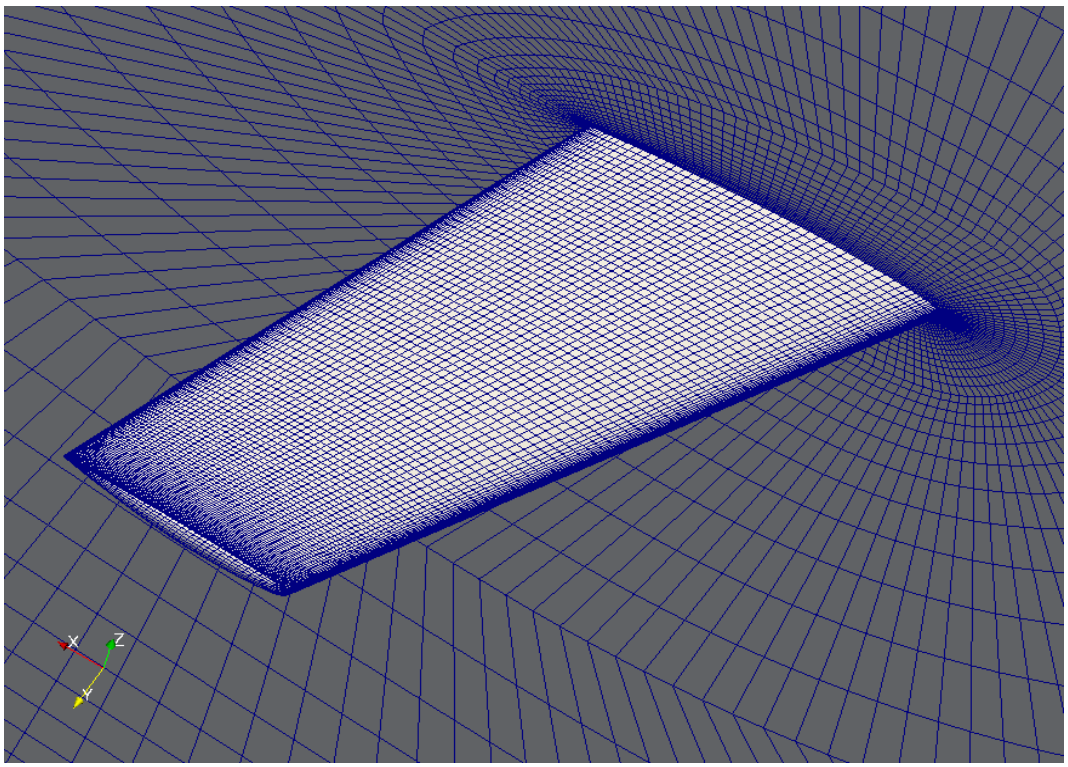

Figure 28: Onera M6 mesh.

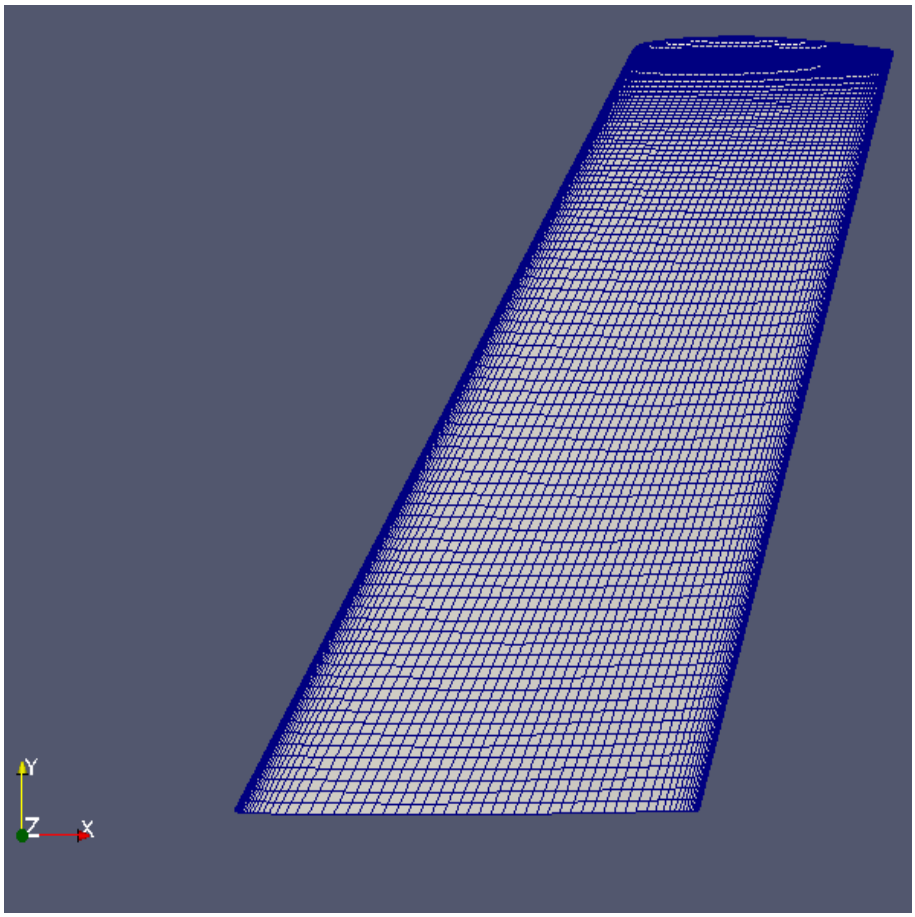

Figure 29: Surface mesh of the Onera M6 wing.

The domain with the boundaries is shown in Figure 30. The blue boundary and the one opposing it are the sides boundaries. The red is the bottom boundary, while the green is the outlet boundary. Opposing the outlet is the inlet, and the bottom is the top boundary. The wing surface is in the yellow section, attached to the boundary shown in blue.

7.2 Results

Six cases were simulated. Three different angles of attack were used, 0°, 5° and 15°. For each angle of attack, a simulation of the original and extended transition models were done. In Figure 31, the experimental results are shown, along with the computations done by Krumbein and Grabe [52], using the original model. Concerning the experimental results, the laminar and turbulent zones were visualized using a sublimation technique based on naphthalene. In Figure 32, the chordwise shear stress at the wall is visualized, obtained by OpenFOAM. The dark blue to dark red represents the lowest to highest values. The transition is in the zones where there is a sudden jump in the wall shear stresses. The brightness of the colors has different values for the different cases, however, the purpose is to visualize the transition zones.

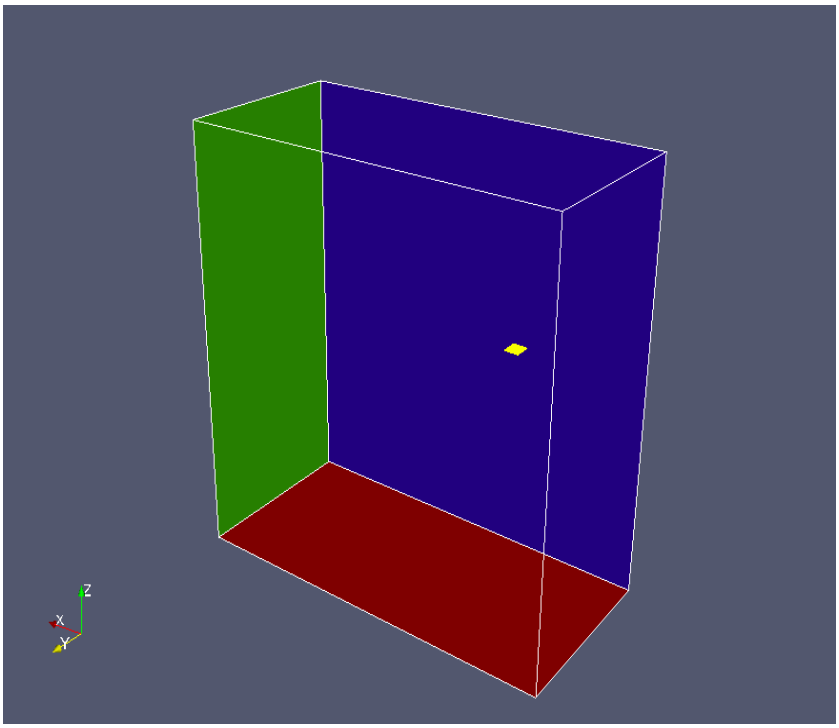

Figure 30: Computational domain

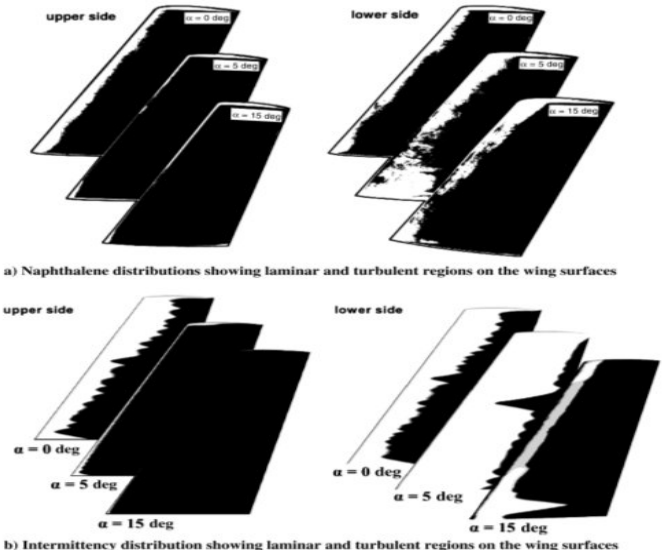

Figure 31: Experimental results with computational result by Krumberin and Grabe [52].

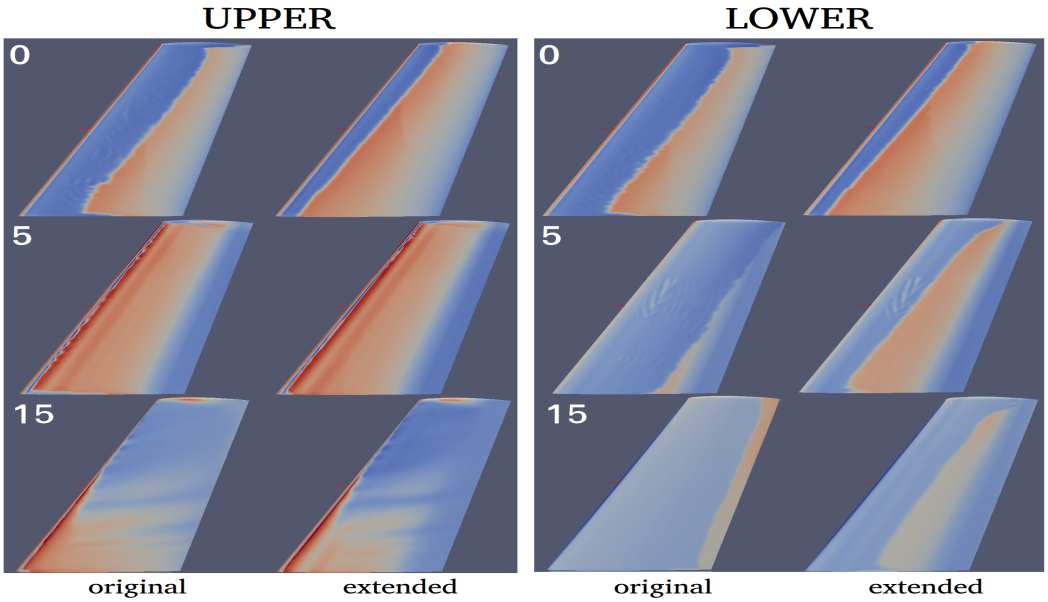

Figure 32: OpenFOAM results.

To get a better picture of the results, the friction coefficient based on the chordwise wall shear stress is plotted along the $x/c = 0.45$, following the publication of Krumberin and Grabe [52], where the transition point onset was evaluated at that cross section. In Figure 33, the position of the airfoil is seen. The plots are presented in Figures 34-36. The pressure coefficient seems unaffected by the extension, as can be seen from Figures 37-39.

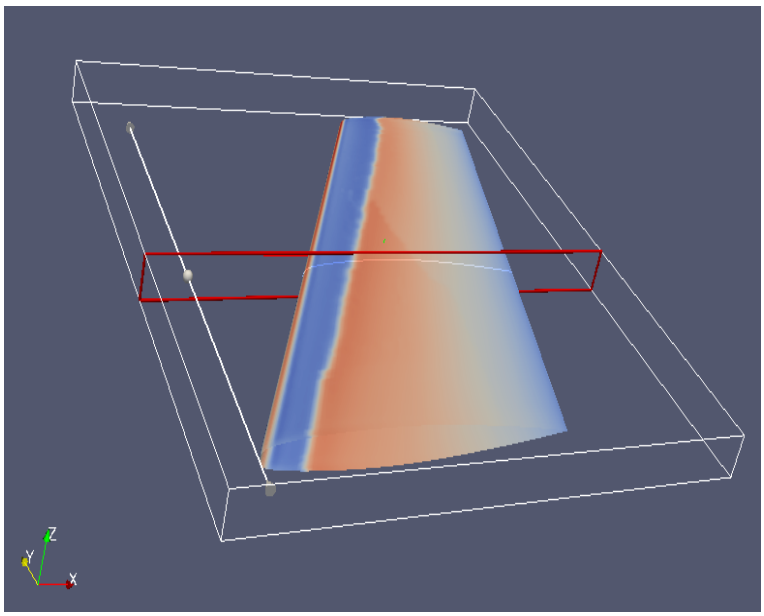

Figure 33: Airfoil position along the span.

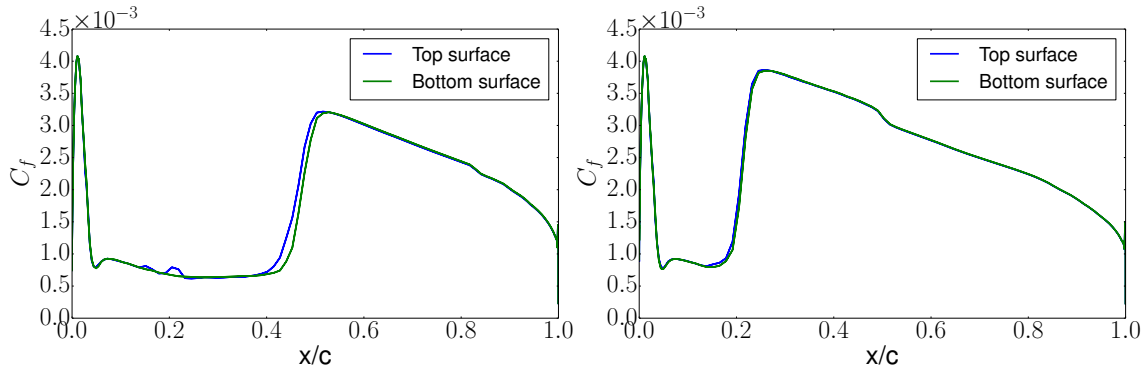

(a) Original. (b) Extended.

Figure 34: Friction coefficient at $\alpha = 0°$.

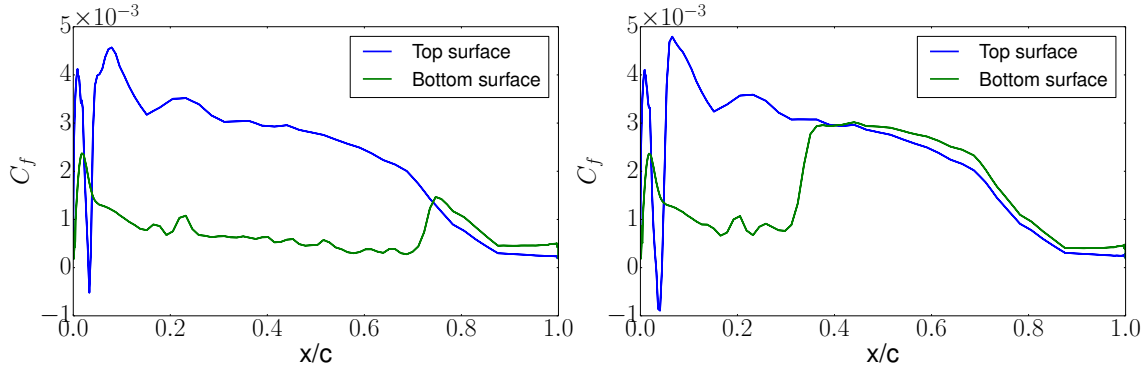

(a) Original. (b) Extended.

Figure 35: Friction coefficient at $\alpha = 5°$.

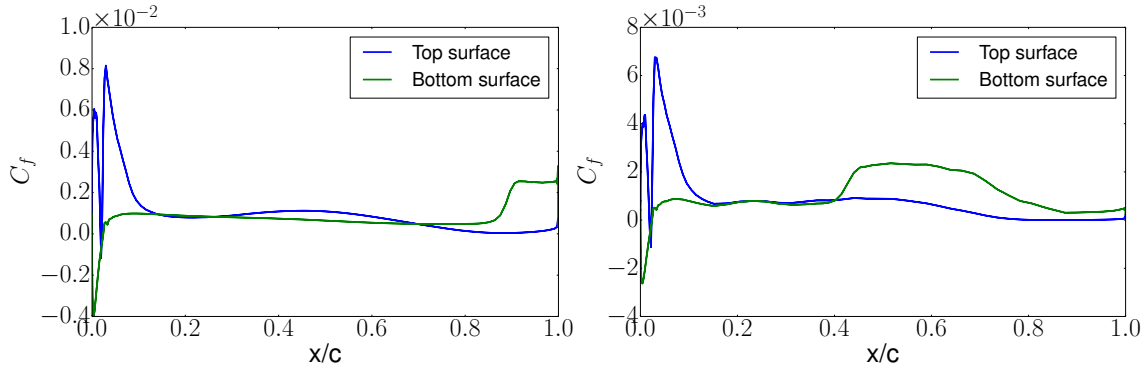

(a) Original. (b) Extended.

Figure 36: Friction coefficient at $\alpha = 15°$.

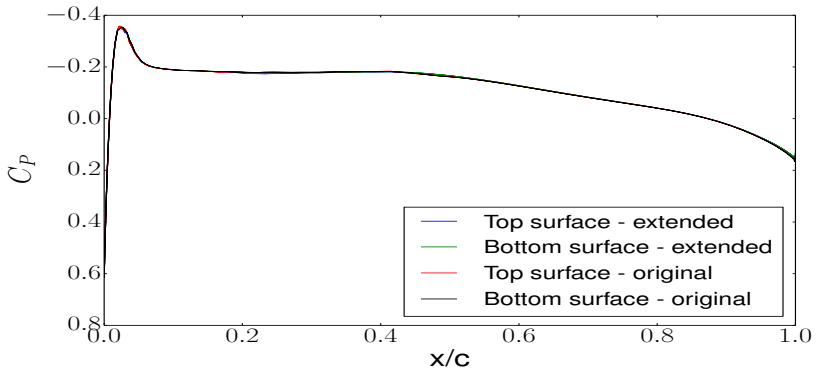

Figure 37: Pressure coefficient at $\alpha = 0°$.

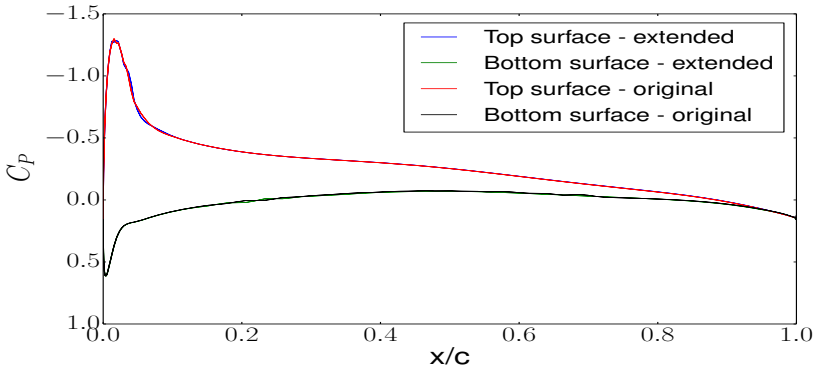

Figure 38: Pressure coefficient at $\alpha = 5°$.

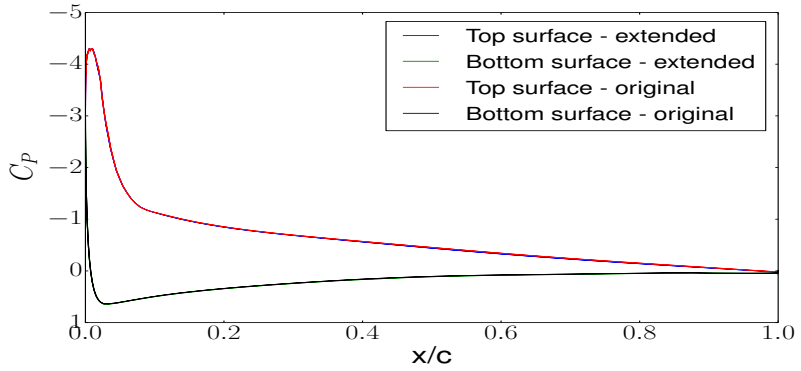

Figure 39: Pressure coefficient at $\alpha = 15°$.

The transition onset points for the different angle of attack are presented in Figure 40. The experimental results are compared with those of Krumbein and Grabe, OpenFOAM original model and extended.

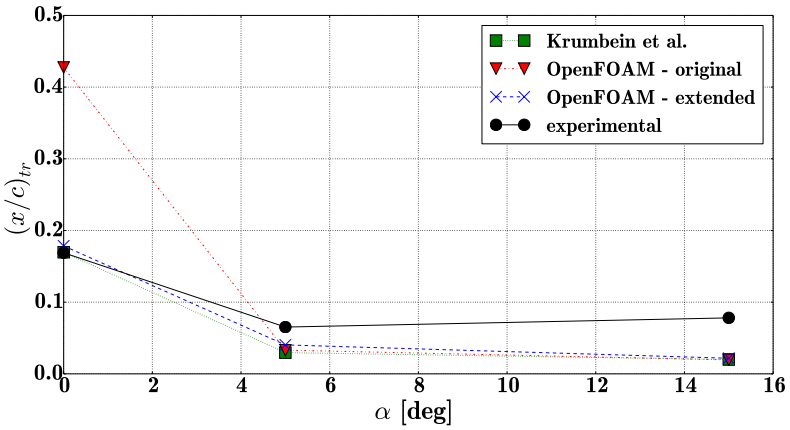

(a) Upper surface

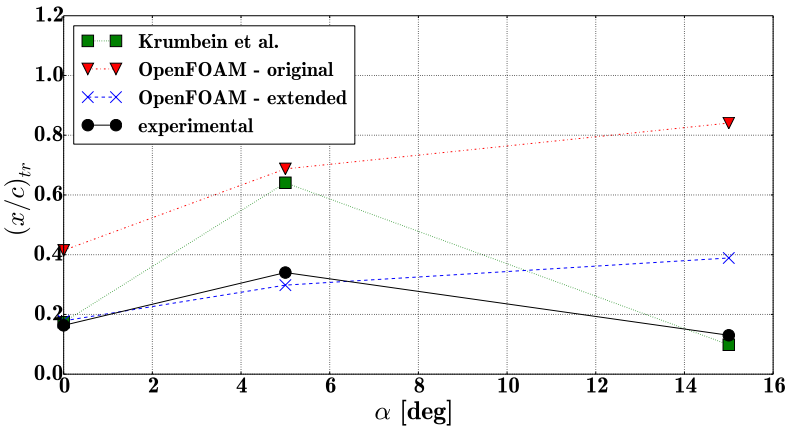

(b) Bottom surface

Figure 40: Transition locations for the ONERA M6 wing at $z/c = 0.45$.

Looking at Figure 40, there is a difference in the results obtained by the original model in the publication by Krumbein and Grabe and those obtained by OpenFOAM in this work. The closest ones are for the case $\alpha = 5°$. The results obtained with the extended model are good for the $\alpha = 0°$ case, somewhat worse for the $\alpha = 5°$ and the worst for the $\alpha = 15°$. Using the extended model, there was not much change on the upper surface except for the $\alpha = 0°$ case. The y^+ distribution for the $\alpha = 0°$ case is shown in Figure 41. The maximum value is $y^+ \approx 5$. For the $\alpha = 5°$, it reaches $y^+ \approx 3$ and for the $\alpha = 15°$, $y^+ \approx 2$. Further lowering the y^+ value has shown almost no changes in the transition onset prediction. The values for the lift and drag coefficients, C_L and C_D respectively, are presented in Table 1. The higher the angle of attack, the smaller the change in the drag coefficient was obtained. The change in the lift coefficient was even less. The airfoil is symmetric, and so, for the $\alpha = 0°$ case, the lift coefficient should be zero.

Table 1: Computed lift and drag coefficients

	Original		Extended	
	C_D	C_L	C_D	C_L
$\alpha = 0°$	0.0054	-0.0000086	0.00728	-0.00036
$\alpha = 5°$	0.0150	0.3037	0.0166	0.3071
$\alpha = 15°$	0.1159	0.8484	0.1184	0.8429

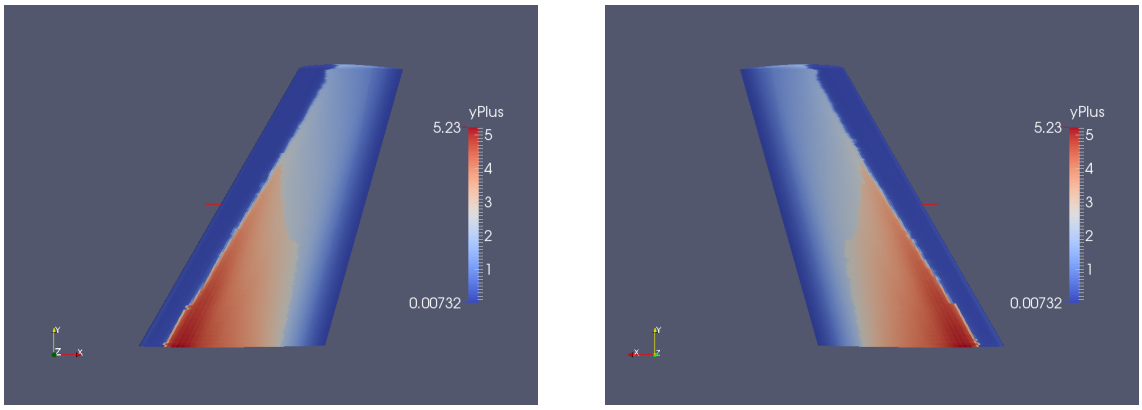

(a) Upper surface (b) Bottom surface

Figure 41: y^+ distribution for $\alpha = 0°$.

All simulation failed to converge, but rather the residual oscillated, as is seen in Figure 42 for the case of $\alpha = 15°$,using the original model.

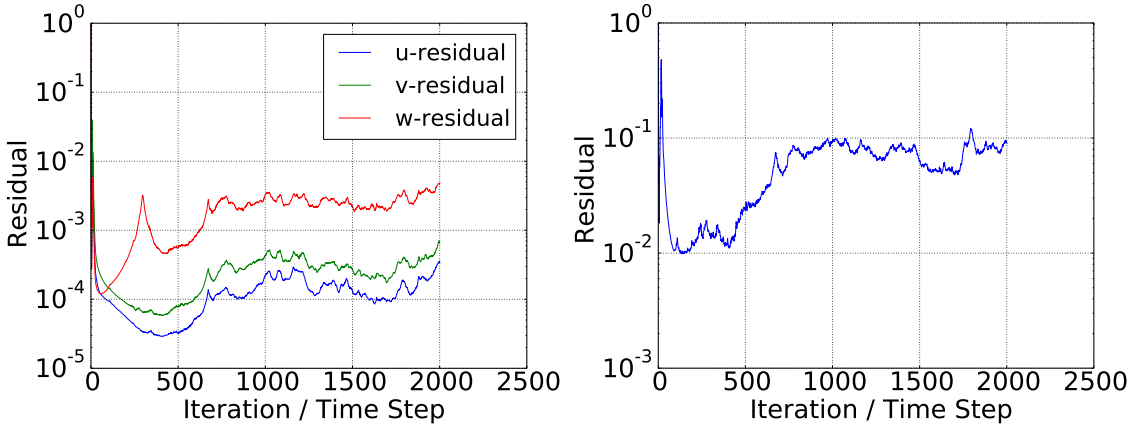

(a) Velocity residual (b) Pressure residual

Figure 42: Convergence for velocity and pressure.

8 Conclusions and Discussion

In this work, a local correlation-based model was extended in the OpenFOAM software to include the effects of roughness- and crossflow-induced transition. The model is based local variables which makes it compatible with modern CFD techniques such as unstructured grids and massive parallel execution. Different transition mechanisms are implemented through empirical correlations. Since laminar to turbulent transition depends on many factors, not all of them were included in the original model. Both extensions, for roughness and crossflow, were introduced separately and tested on some known cases.

The roughness-extended model has shown very high sensitivity to freestream turbulence. The best results were obtained for the adverse-pressure gradient in terms of transition onset prediction. The worst were obtained for the zero-pressure gradient. The reasoning for this could be that the effects of freestream turbulence were not so strong because of the pressure gradient. The best prediction for the wall shear stress was obtained for the zero-pressure gradient and worst for the favorable-pressure gradient. This could be due to the fact that a much higher freestream turbulence was applied for the favorable-pressure gradient in the work Langel and Chow [6]. Since two different implementations of the transition model were available, it was found that the manner in which the transition model is implemented has an affect on the behavior of the roughness-extended model. The implementation of the transition model could be reason of the difference in the results.

In the crossflow-extended model, good results were obtained for the $\alpha = 0°$ case, somewhat worse for the $\alpha = 5°$, and the worst for the $\alpha = 15°$ case compared to the experimental results. The OpenFOAM results were compared to the publication of Krumbein and Grabe, where only the original model was used on the Onera M6 case. There were differences in the results of the original model used by Krumbein and Grabe and the one implemented in OpenFOAM. This could be explained by the differences in the implementation.

The OpenFOAM implementation should be further validated. Perhaps in the future, the focus should be on the new model, published in 2015 by Menter et al. [5], which is Galilean invariant. According to the authors, a crossflow-induced transition criteria has already been implemented. The concept for the roughness extension presented in this work could possibly be applied also on this new model. The paper by Saeed et al. [53] could be used for comparison, where the combined effects of crossflow and roughness could be tested. Additional effects could be added, such as freestream turbulent length scale, streamline curvature and Mach number effects, which are also not included in the base model used in this thesis.

References

[1] Hellsten, A., *New Two-Equation Turbulence Model for Aerodynamics Applications*. PhD thesis, Helsinki University of Technology, Espoo, Finland, February 2004. ISBN 951-22-6933-3 (print), 951-22-6934-1 (pdf, available at http://lib.hut.fi/Diss/).

[2] Langtry, R. B., *A correlation-based transition model using local variables for unstructured parallelized CFD codes*. PhD thesis, University of Stuttgart, 2006.

[3] Walters, D. K. and Cokljat, D., "A three-equation eddy-viscosity model for Reynolds-averaged Navier–Stokes simulations of transitional flow," *Journal of fluids engineering*, Vol. 130, No. 12, 2008, p. 121401.

[4] Menter, F., Esch, T., and Kubacki, S., "Transition modelling based on local variables," in *5th International Symposium on Turbulence Modeling and Measurements, Mallorca, Spain*, 2002.

[5] Menter, F. R., Smirnov, P. E., Liu, T., and Avancha, R., "A One-Equation Local Correlation-Based Transition Model," *Flow, Turbulence and Combustion*, Vol. 95, No. 4, 2015, pp. 583–619.

[6] Langel, C. M., Chow, R., Dam, C., Maniaci, D., Ehrmann, R. S., and White, E. B., "A computational approach to simulating the effects of realistic surface roughness on boundary layer transition," 2014, pp. 1–16.

[7] Müller, C. and Herbst, F., "Modelling of crossflow-induced transition based on local variables," *Proc. ECCOMAS, Paper*, No. 2252, 2014.

[8] Schlichting, H., *Boundary-Layer Theory*. McGraw-Hill, New York, 1979.

[9] "Which Turbulence Model Should I Choose for My CFD Application?." https://www.comsol.com/blogs/which-turbulence-model-should-choose-cfd-application/. Accessed: 2016-04-6.

[10] Houghton, E. L. and Carpenter, P. W., *Aerodynamics for engineering students*. Butterworth-Heinemann, 2003.

[11] Turunen, T. *et al.*, "Analysis of multi-propeller marine applications by means of computational fluid dynamics," Master's thesis, Aalto University, 2014.

[12] White, F. M., *Viscous fluid flow*. Singapore: McGraw-Hill Book Co., 3rd ed., 2006. ISBN 0–07–124493–X.

[13] Medida, S., *Correlation-based transition modeling for external aerodynamic flows*. PhD thesis, University of Maryland, 2014.

[14] Morkovin, M. V., "On the many faces of transition," in *Viscous drag reduction*, pp. 1–31, Springer, 1969.

[15] Saric, W. S., Reed, H. L., and Kerschen, E. J., "Boundary-layer receptivity to freestream disturbances," *Annual review of fluid mechanics*, Vol. 34, No. 1, 2002, pp. 291–319.

[16] Schubauer, G. B. and Skramstad, H. K., "Laminar-boundary-layer oscillations and transition on a flat plate," National Bureau of Standards; Washington, DC, United States, Laboratory of Aerodynamics, 1948.

[17] Durbin, P. A. and Reif, B. P., *Statistical theory and modeling for turbulent flows*. John Wiley & Sons, 2011.

[18] Spalart, P. and Shur, M., "On the sensitization of turbulence models to rotation and curvature," *Aerospace Science and Technology*, Vol. 1, No. 5, 1997, pp. 297–302.

[19] Finnis, M. and Brown, A., "Stability of a laminar boundary layer flowing along a concave surface," *Journal of Turbomachinery*, Vol. 111, No. 4, 1989, pp. 376–386.

[20] Saric, W. S., Carrillo, R. B., and Reibert, M. S., "Nonlinear stability and transition in 3-D boundary layers," *Meccanica*, Vol. 33, No. 5, 1998, pp. 469–487.

[21] Reed, H. L. and Saric, W. S., "Stability of three-dimensional boundary layers," *Annual Review of Fluid Mechanics*, Vol. 21, No. 1, 1989, pp. 235–284.

[22] Sengupta, T. K., *Theoretical and Computational Aerodynamics*. John Wiley & Sons, 2014. ISBN: 978-1-118-78759-5.

[23] Reed, H. L., "Wave interactions in swept-wing flows," *Physics of Fluids (1958-1988)*, Vol. 30, No. 11, 1987, pp. 3419–3426.

[24] Langel, C. M., Chow, R., Dam, C., Maniaci, D., Ehrmann, R. S., and White, E. B., "Modeling of Roughness Induced Transition Using a Local Correlation Method," 2014.

[25] Gibbings, J., "On boundary-layer transition wires," Department of Fluid Mechanics, University of Liverpool, 1959.

[26] White, E. B. and Saric, W. S., "Application of variable leading-edge roughness for transition control on swept wings," *AIAA paper*, Vol. 283, 2000, p. 2000.

[27] William, S., Ruben Jr, B., *et al.*, "Leading-edge roughness as a transition control mechanism," in *36th AIAA Aerospace Sciences Meeting and Exhibit*, 1998.

[28] Greenshields, C. J., "The open source CFD Toolbox User guide, Version 3.0.1," OpenFOAM Foundation Ltd., 2015.

[29] Wilcox, D. C. *et al.*, *Turbulence modeling for CFD*, Vol. 2. DCW industries La Canada, CA, 1998.

[30] Menter, F. R., "Two-equation eddy-viscosity turbulence models for engineering applications," *AIAA journal*, Vol. 32, No. 8, 1994, pp. 1598–1605.

[31] Wilcox, D. C., "Reassessment of the scale-determining equation for advanced turbulence models," *AIAA journal*, Vol. 26, No. 11, 1988, pp. 1299–1310.

[32] Launder, B. E. and Spalding, D., "The numerical computation of turbulent flows," *Computer methods in applied mechanics and engineering*, Vol. 3, No. 2, 1974, pp. 269–289.

[33] Eymard, R., Gallouët, T., and Herbin, R., "Finite volume methods," *Handbook of numerical analysis*, Vol. 7, 2000, pp. 713–1018.

[34] Versteeg, H. K. and Malalasekera, W., *An introduction to computational fluid dynamics: the finite volume method*. Pearson Education, 2007.

[35] Patankar, S. V. and Spalding, D. B., "A calculation procedure for heat, mass and momentum transfer in three-dimensional parabolic flows," *International journal of heat and mass transfer*, Vol. 15, No. 10, 1972, pp. 1787–1806.

[36] Issa, R. I., "Solution of the implicitly discretised fluid flow equations by operator-splitting," *Journal of computational physics*, Vol. 62, No. 1, 1986, pp. 40–65.

[37] "OpenFOAM guide/The SIMPLE algorithm in OpenFOAM." `https://openfoamwiki.net/index.php/OpenFOAM_guide/The_SIMPLE_algorithm_in_OpenFOAM`. Accessed: 2016-04-5.

[38] Behrens, T., "OpenFOAM's basic solvers for linear systems of equations," *Chalmers, Department of Applied Mechanics*, Vol. 18, No. 02, 2009.

[39] Langtry, R. B. and Menter, F. R., "Correlation-based transition modeling for unstructured parallelized computational fluid dynamics codes," *AIAA journal*, Vol. 47, No. 12, 2009, pp. 2894–2906.

[40] Malan, P., Suluksna, K., and Juntasaro, E., "Calibrating the γ-Reθ transition model for commercial CFD," in *47th AIAA Aerospace Sciences Meeting*, pp. 5–8, 2009.

[41] Nikulainen, J., "Implementation of a Local Correlation-Based Transition Model for FINFLO Flow Solver," 2012.

[42] Van Driest, E. and Blumer, C., "Boundary Layer Transition–free-stream Turbulence and Pressure Gradient Effects," DTIC Document, 1963.

[43] Seyfert, C. and Krumbein, A., "Correlation-based transition transport modeling for three-dimensional aerodynamic configurations," *AIAA Aerospace Science Meeting*, 2012.

[44] Watanabe, Y., Misaka, T., Obayashi, S., Arima, T., and Yamaguchi, Y., "Application of Crossflow Transition Criteria to Local Correlation-Based Transition Model," in *47th AIAA Aerospace Sciences Meeting*, No. 2009-1145, 2009.

[45] Dassler, P., Kožulović, D., and Fiala, A., "Modelling of Roughness-Induced Transition Using Local Variables," in *V European Conference on CFD, ECCOMAS CFD*, 2010.

[46] "MSc/PhD course in CFD with OpenSource software, 2012." `http://www.tfd.chalmers.se/~hani/kurser/OS_CFD_2012/AyyoobZarmehri/SSTtransition_ayyoob_zarmehri_slides.pdf`. Accessed: 2016-04-5.

[47] Langfeldt, F., "correlation-based turbulence model with transition for OpenFOAM." `https://github.com/langfeldt/gammaReThetatSST`. Accessed: 2016-04-5.

[48] Schmitt, V. and Cousteix, J., "Étude de la couche limite tridimensionelle sur une aile en flèche," *ONERA, Rapport Technique*, No. 14/1713, 1975.

[49] Rahman, U. A. and Mustapha, F., "Validations of OpenFoam Steady State Compressible Solver Rhosimplefoam," in *International Conference on Mechanical and Industrial Engineering*, 2015.

[50] Sweby, P. K., "High resolution schemes using flux limiters for hyperbolic conservation laws," *SIAM journal on numerical analysis*, Vol. 21, No. 5, 1984, pp. 995–1011.

[51] Sim, T. S., Ong, M. C., Quek, W. Y., Sum, Z. W., Lai, W. X., and Skote, M., "A numerical study of microburst-like wind load acting on different block array configurations using an impinging jet model," *Journal of Fluids and Structures*, Vol. 61, 2016, pp. 184–204.

[52] Grabe, C. and Krumbein, A., "Correlation-based transition transport modeling for three-dimensional aerodynamic configurations," *Journal of Aircraft*, Vol. 50, No. 5, 2013, pp. 1533–1539.

[53] Saeed, T., Morrison, J., and Mughal, M., "Roughness effects on swept-wing crossflow transition in moderate free-stream turbulence,"

[54] "MSc/PhD course in CFD with OpenSource software, 7.5hec , 2015." `http://www.tfd.chalmers.se/~hani/kurser/OS_CFD/highLevelProgramming.pdf`. Accessed: 2016-04-5.

A OpenFOAM Implementation

A.1 Programming in OpenFOAM

The benefit of C++ is that it is object-oriented, and thus provides the mechanism-classes-to declare types and associated operations that are part of the verbal and mathematical languages used in science and engineering. The C++ class library gives the possibility to implement complicated physical and mathematical models as high-level mathematical expressions.

There are two types of tensor-derivative classes implemented in OpenFOAM:

- fvm(finite volume method) for implicit equations
- fvc(finite volume calculus) for explicit equations

As an explicit equation can be solved immediately, the fvc does that. Given an operation on a volume field, the fvc namespace produced another volume field. The fvm namespace will discretize the term into the matrix equations, and return matrix coefficients.

Some functions are presented in Figure A1:

Term description	Implicit/explicit	Mathematical expression	fvm::/fvc:: functions
Laplacian	Implicit/Explicit	$\nabla \cdot \Gamma \nabla \phi$	laplacian(Gamma,phi)
Time derivative	Implicit/Explicit	$\partial\phi/\partial t$	ddt(phi)
		$\partial\rho\phi/\partial t$	ddt(rho, phi)
Convection	Implicit/Explicit	$\nabla \cdot (\psi)$	div(psi, scheme)
		$\nabla \cdot (\psi\phi)$	div(psi, phi, word)
			div(psi, phi)
Source	Implicit	$\rho\phi$	Sp(rho, phi)
	Implicit/Explicit		SuSp(rho, phi)

ϕ: vol<type>Field, ρ: scalar, volScalarField, ψ: surfaceScalarField

Figure A1: Functions in OpenFOAM [54].

As an example, a partial differential equation:

$$\frac{\partial \rho U}{\partial t} + \nabla \cdot \phi U - \nabla \cdot \nu \nabla U = -\nabla p \tag{A1}$$

can be represented in the following way in OpenFOAM:

```
solve
(
fvm::ddt(rho, U)
+ fvm::div(phi, U)
- fvm::laplacian(mu, U)
==
- fvc::grad(p)
);
```

A.2 Model Implementation

A.2.1 Roughness Effects

In order to implement the model, a transport equation had to be implemented. Following the OpenFOAM syntax, the equation is written.

```
tmp<fvScalarMatrix> ArEqn
    (
        fvm::ddt(Ar_)
      + fvm::div(phi_, Ar_)
      - fvm::Sp(fvc::div(phi_), Ar_)
      - fvm::laplacian(DArEff(), Ar_)

    );
    ArEqn().relax();
    solve(ArEqn);
```

Since F_{Ar} depends on A_r, the following lines are used:

```
forAll(Ar_, cellI)
        {

         if (Ar_[cellI]< sqrt((2.0)/(3.0*0.0005)))
            {F_Ar[cellI]= 0.0005*Foam::pow(Ar_[cellI],3.0);
             }
         else if (Ar_[cellI]>=sqrt((2.0)/(3*0.0005)))
            {F_Ar[cellI]=2.0*(Ar_[cellI] - sqrt(2.0/(3.0*0.0005))) + 0.0005*
             Foam::pow(sqrt(2.0/(3.0*0.0005)),3.0) ;
             }

        }
```

The production term is altered in the following way:

$$P_{\theta t} = c_{\theta t}\frac{\rho}{t}[(Re_{\theta t} - Re_{\theta t})(1 - F_{\theta t}) - F_{Ar}] \tag{A2}$$

It is implemented in the following way:

```
cThetat_*magSqr(U_)*(scalar(1.0)-FThetat())*ReThetatField/(scalar(500.0)*nu())
      - fvm::Sp(cThetat_*magSqr(U_)*(scalar(1.0)-FThetat())/(scalar(500.0)*nu()),
      ReThetatTilda_)-F_Ar*0.03*Foam::pow(mag(U_),2.0)/(500.0*nu())
```

Boundary Conditions

The boundary condition for ω and k^+ had to be implemented in OpenFOAM. This was done suing the groovyBC library. The k^+ from Eq. (98) is implemented as:

```
flatPlate
    {
    type            groovyBC;
   valueExpression "8*((ks)/(0.000015))*sqrt((0.000018)*mag(snGrad(U))/1.2)";
    value           uniform  0;

   }
```

where in the place of k_s, the roughness height is specified
The modified boundary for ω, from Eq. (94) is implemented as:

```
        flatPlate
 {
         type                          groovyBC;
    valueExpression            "(kp >25) ? (0.000018*mag(snGrad(U))/1.2)*
    (100/kp)/0.000015 : (0.000018*mag(snGrad(U))/1.2)*(50/kp)*(50/kp)/0.000015 ";
    variables                  "kp=(ks/0.000015)*sqrt(0.000018*mag(snGrad(U))/
                                 1.2 );";
   value                        300;
    }
```

A.2.2 CrossFlow Effects

In order to implement the source term, some terms need to be defined.

first, θ is defined:

$$\theta = \frac{Re_v \nu}{2.193 U \rho} \tag{A3}$$

In OpenFOAM, it is written as:

```
tmp<volScalarField> gammaReThetatSST::Theta() const
{
    return ((mag(symm(fvc::grad(U_)))*Foam::pow(y_,2.0)+mindis)/
    (nu())*nu())/(scalar(2.193)*mag(U_)+minvel);
}
```

The Helicity Reynolds number :

$$Re_H = \frac{\theta}{\nu}\sqrt{\theta H} \tag{A4}$$

```
tmp<volScalarField> gammaReThetatSST::ReH() const
{
    return sqrt(Theta()*(mag(U_ & fvc::curl(U_))))*(Theta()/nu());
}
```

The Reynolds number:

$$Re_{\Omega} = \frac{\rho y^2}{\nu}\Omega \tag{A5}$$

```
tmp<volScalarField> gammaReThetatSST::ReOM() const
{
    return (mag(skew(fvc::grad(U_)))*Foam::pow(y_,2.0))/(nu());
}
```

The source term added is:

$$P_{\theta t,mod} = c_{\theta t}\frac{\rho}{t}[(Re_{\theta t} - Re_{\theta t})(1 - F_{\theta t}) - F_{Ar}] \tag{A6}$$

```
min(max(unit*scalar(0),60*pow((ReH()/6),
scalar(0.548))*pow(ReOM(),scalar(0.1912))*magSqr(U_)/
(scalar(1000)*scalar(500)*nu())),scalar(1666.5)*unit)
```